Microwave-Based Controlled Quantum Dynamics in Trapped Ions

Gatis Mikelsons

Department of Physics

Imperial College London

A thesis submitted for the degree of

Doctor of Philosophy

December 2014

Abstract

The key research aim of the present thesis is the building of a universal set of quantum gates for a long wavelength trapped-ion quantum information processor. It is desired to realise quantum computation using microwave and radio wave sources in a linear ion trap, where a static magnetic field gradient has been added to enhance motional and atomic state coupling. Furthermore, the qubit is constructed with the intrinsic use of superposition states generated with the help of constant microwave fields in the background: dressed states. This technique is essential for the shielding of the quantum operations against the unavoidable effects of magnetic noise.

After reviewing the preliminary results and discussing briefly an auxiliary experimental technique intrinsic to the set-up, we introduce the magnetic gradient coupling and the dressed state scheme. We then proceed to illustrate how single and multi-qubit gates can be realised within such a system. Theoretical arguments are supplemented by numerical simulation and sources of experimental noise are taken into account.

Contents

List of Figures

I hereby declare that this thesis and the work reported herein was composed by and originated entirely from me, under confirmed supervision and assistance. Information derived from the published and unpublished work of others has been acknowledged in the text and references are given in the References section.

Acknowledgements

I would like to thank all the people who have sustained me by helpful action and often just by a simple presence throughout this years-long climb in the mountains.

List of abbreviations

The following abbreviations are employed through the text:

BCH - Baker-Campbell-Hausdorff (formula)

MW - microwave (frequency)

RF - radio frequency

RWA - Rotating wave approximation

SHO - simple harmonic oscillator

STIRAP - Stimulated Raman adiabatic passage

TDSE - Time-dependent Schrödinger equation

Chapter 1

Introduction

Building a fully functional quantum processor is one of the most exciting challenges of present-day physics, both on the theoretical and the experimental side. Not only would a quantum computer enable efficient tackling of problems intractable on the classical analogue; it also holds the promise to shed more light on the elusive transition between quantum and classical physics (see e.g. Johanning et al. [2009a]; Nielsen and Chuang [2010]; Wunderlich and Balzer [2003] and the references therein). Even a small number of qubits could enable a processor to be built with computing capabilities superiour to those of the classical computer.

Trapped and laser-cooled ions have been shown, over the past two decades, to be one of the most promising candidates for the implementation of a quantum processor. A paper by Cirac et al. [1995] can be considered to be the initial breakthrough for the field. In this study, the authors demonstrated the feasibility of both single-qubit and multi-qubit quantum gates, thus arguing that a universal quantum computer could in principle be implemented using this physical system.

Since then, the field of trapped-ion quantum computing has seen countless developments, both theoretical and experimental. On the theoretical side, a multitude of alternative entangling gates and set-ups have been proposed (Milburn et al. [2000]; Roos [2008]; Sørensen and Mølmer [1999]). On the experimental side, many achievements would deserve mention. The implementation of the two-qubit CNOT gate, following the Cirac-Zoller scheme, was performed by Schmidt-Kaler et al. [2003a,b] and Riebe et al.

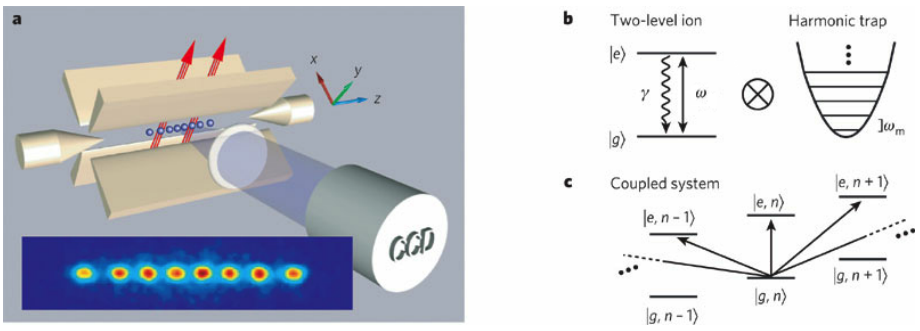

Figure 1.1: Realising quantum computation with trapped ions (Blatt and Wineland [2008]). Detailed explanation of the panels is provided in the text.

[2006]. Experimental creation of the Bell states and their arbitrary superpositions has been performed by Rowe et al. [2001] and Roos et al. [2004b]. Maximally entangled states of up to eight qubits have been created and analysed (Häffner et al. [2005]; Leibfried et al. [2005]; Roos et al. [2004a]), with still more experimental progress in recent years (Monz et al. [2011]). As a final example in this sparse list, the quantum teleportation protocol has been successfully implemented and demonstrated (Barrett et al. [2004]; Riebe et al. [2004]).

Figure 1.1 (Blatt and Wineland [2008]) summarises the common features of many of these experiments and serves as the best introduction for the present research work. Panel **a** shows a string of ions stored in a linear quadrupole trap (linear Paul trap) represented by the beige electrodes. Strong confinement in the $x-y$ plane is accomplished by a time-dependent quadrupole field. Confinement in the z direction is created by a further pair of electrodes, which counteract the ions' mutual Coulomb repulsion. A shared normal-mode motion along the z direction is thus created. Laser addressing of individual ions for cooling and quantum dynamics is achieved by tightly-focused laser beams (red). In a typical experiment, the spacing of ions in the displayed image is on the order of few μm, and the string would be cooled down to the ground state or a low-lying excited state of a shared motional mode.

Each ion is used to represent a single qubit by choosing two particular electronic configurations to stand for the logical $|g\rangle$ and $|e\rangle$ states. Quan-

tum dynamics can be achieved by addressing this two-level system by lasers of appropriate duration and frequency. Communication between individual qubits is achieved via the shared motional mode (the 'bus qubit'), which is described quantum mechanically as the simple harmonic oscillator (SHO), with energy levels of particular spacing.

Panels **b** and **c** of Figure 1.1 illustrate this set-up in detail. Panel **b** shows the quantum-mechanical representation of the state of a single qubit embedded in a shared motional mode. The complete state is represented as the tensor product of the electronic state (in a space spanned by $|g\rangle$ and $|e\rangle$) and the phonon state (in a space spanned by $|n\rangle$, where n represents the phonon number).

For cooling of the ion chain and for the purpose of achieving communication between different qubits, it is crucial to have the capacity to excite transitions involving changes in the phonon number n. Given that the motional mode is shared between all particles in the trap, such 'sideband coupling' allows for communication between different qubits. Schemes for realising multi-qubit gates, such as the Cirac-Zoller scheme (Cirac et al. [1995]), rely on this idea. Panel **c** of Figure 1.1 illustrates the kind of interactions that would be used. It is desired to achieve coupling between the ground and excited states of an ion (i) without a change in the phonon number (carrier), (ii) with a reduction of the phonon number by 1 (red sideband), and (iii) with an increase in the phonon number by 1 (blue sideband). Careful application of such pulses enables both single-qubit and multi-qubit quantum gates to be realised.

While many milestones in the field of trapped-ion quantum information processing have been reached, the scientific endeavor is still in progress. In particular, it is of interest to design quantum gates that would utilise microwave (MW) and radio frequency (RF) fields, instead of the laser light. Such a step would simplify significantly the experimental burden. Numerous other difficulties (noise isolation, individual laser focusing, miniaturisation, moving individual qubits across in space, etc.) need solution by clever design and technique.

A proposal to perform quantum computation in trapped ions using long-wavelength radiation and electronic superposition states for encoding the logical qubit (Timoney et al. [2011]) promises to overcome some of

these obstacles. It is the purpose of this dissertation to demonstrate mathematically the feasibility of universal quantum computation within this 'dressed-state' setting. We develop in detail this research idea and show how both single and multi-qubit quantum gates of desirable properties can be implemented.

The thesis contains both original research work and rephrasing of useful theoretical and experimental results from other people's previous publications. To help separate the two (apart from the referencing), the introductory text for each chapter will contain a paragraph outlining what content is original and which content amounts to a summary of known results.

Chapter 2

Preliminaries

This chapter introduces a number of results and models from quantum mechanics and atomic physics that will be used throughout the remainder of the text. Useful notation is introduced and several standard derivations are presented for clarity and reference. Moreover, the physical system of most relevance to the present research work - trapped $^{171}Yb^{+}$ ions - is also described.

The content of this chapter is entirely a summary of known results. Only the figures and the presentation amount to original material.

2.1 The dipole Hamiltonian and the two-level system

As the first key result, the dipole Hamiltonian is presented, which models the interaction between the electronic quantum states of an atom and a classical electromagnetic driving field. The dipole Hamiltonian will be of crucial importance for the research work discussed.

Firstly, the derivation of the dipole Hamiltonian will be outlined, stating explicitly the approximations made. Secondly, the case of a two-level system interacting with an external field will be examined in detail, introducing the rotating wave approximation and the phenomenon of Stark shift.

2.1.1 Dipole Hamiltonian

The laser-atom interaction is modeled in a semi-classical fashion, considering quantum-mechanical atomic states interacting with a classical light field. The derivation outlined in this section follows closely the treatment by Gerry and Knight [2005].

In the absence of external fields, the Hamiltonian for an electron bound to an atom can be written as:

$$H_f = \frac{\mathbf{p}^2}{2m_e} + V(r) \tag{2.1}$$

where $\mathbf{p}$ represents the momentum operator, m_e is the electron mass, and $V(r)$ is the Coulomb potential. The external electromagnetic field is introduced by means of the vector potential $\mathbf{A}(\mathbf{r}, \mathrm{t})$ and the scalar potential $\phi(\mathbf{r}, t)$. Taking e to be the (positive) magnitude of the electron charge, the free Hamiltonian needs to be rewritten to introduce the electromagnetic field:

$$H_{EM} = \frac{(\mathbf{p} + e\mathbf{A})^2}{2m_e} - e\phi + V(r). \tag{2.2}$$

Two approximations are now made to manipulate algebraically the Hamiltonian (2.2) into a simple form. Firstly, the Coulomb gauge for the electromagnetic field is assumed, implicitly restricting the model to non-relativistic contexts. Secondly, the 'dipole approximation' is applied:

$$\mathbf{k} \cdot \mathbf{r} \ll 1. \tag{2.3}$$

Here, $\mathbf{k}$ is the wave vector of the electromagnetic radiation and $\mathbf{r}$ is the position vector. Effectively, it is assumed that, over the physical size of the electron configuration, the electromagnetic field can be assumed to be spatially invariant and therefore only time-dependent. This is a good approximation for the typical atom sizes and optical or longer-wavelength radiation. With these approximations and after algebraic manipulation involving a definite gauge transformation, one derives:

$$H_d = \frac{\mathbf{p}^2}{2m_e} + V(r) + e\mathbf{r} \cdot \mathbf{E}(t). \tag{2.4}$$

It is seen that, compared to the free Hamiltonian (2.1), a single additional interaction term is introduced, which is typically referred to as the dipole coupling. Hamiltonian (2.4) will provide the starting point for modeling the interactions discussed throughout the proceeding chapters. Introducing the dipole operator $\mathbf{d} = -e\mathbf{r}$, the interaction Hamiltonian can also be rewritten as:

$$H_I = -\mathbf{d} \cdot \mathbf{E}(t) \tag{2.5}$$

so that the complete Hamiltonian is given by:

$$H_d = H_f + H_I. \tag{2.6}$$

To study the properties of a laser-atom system, the Hamiltonian H_d can be expanded in the basis of the eigenstates of the free atomic Hamiltonian H_f (2.1). A diagonal set of terms will be recovered, corresponding to the free part, together with the matrix elements of H_I in between the free eigenstates. By parity considerations, H_I will only give rise to off-diagonal terms (Keaveney [2014]). Any pair of atomic states that does generate non-zero off-diagonal terms will be coupled within the dipole approximation and therefore liable to undergo transitions. This consideration can be used to find the 'allowed' and 'forbidden' transitions.

The electric dipole Hamiltonian derived above represents the dominating semi-classical form of interaction between electronic quantum states and light fields. However, other interaction terms are recovered as well, in a more detailed analysis, such as magnetic and quadrupole terms. The hyperfine $^{171}Yb^{+}$ transitions considered in later chapters, for example, rely on the magnetic dipole interaction term (Wunderlich and Balzer [2003]). However, such transitions lead to the same type of interaction Hamiltonian as presented below (2.7).

2.1.2 Rabi frequency and the Rotating wave approximation

This section introduces the standard approximation that is often applied to the dipole Hamiltonian. Also, the parameter for the interaction strength -

the 'Rabi frequency' - will be introduced and defined. One considers a two-level atomic system of free Hamiltonian eigenstates $|u\rangle$ and $|d\rangle$ (Figure 2.1), with non-zero matrix element for the interaction Hamiltonian H_I (2.5).

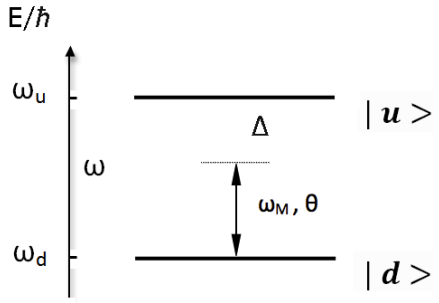

Figure 2.1: Two-level system with laser addressing. Level energies and laser parameters are indicated.

The free and interacting parts of the Hamiltonian can be written as:

$$H_f = \begin{matrix} \\ |u\rangle \\ |d\rangle \end{matrix} \begin{matrix} \begin{matrix} \langle u| & \langle d| \end{matrix} \\ \begin{pmatrix} \hbar\omega_u & 0 \\ 0 & \hbar\omega_d \end{pmatrix} \end{matrix} \quad , \quad H_I = \hbar\Omega \begin{pmatrix} 0 & \cos(\omega_M t + \theta) \\ \cos(\omega_M t + \theta) & 0 \end{pmatrix} \tag{2.7}$$

Here, one has assumed the electric field to be of sinusoidal form and aligned along a particular axis called y. In line with the dipole approximation (2.3), we have omitted the term in the $\cos(..)$ function containing the wave number k, so that the electric field is specified as:

$$\mathbf{E}(t) = \mathbf{u}_y \cdot \mathcal{E}(t) \cos(\omega_M t + \theta). \tag{2.8}$$

And we have defined the Rabi frequency Ω via evaluating the interaction Hamiltonian H_I in between the two free-Hamiltonian eigenstates:

$$\begin{aligned} \langle u|e\mathbf{r} \cdot \mathbf{E}(\mathrm{t})|d\rangle &= \langle u|e \cdot y|d\rangle \, \mathcal{E}(t) \, \cos(\omega_M t + \theta) \\ &= \hbar\Omega(t) \, \cos(\omega_M t + \theta) \end{aligned} \tag{2.9}$$

Ω is the parameter governing the strength of the laser-atom interaction. It is proportional to the amplitude of the laser field. Moreover, the Rabi

frequency Ω encapsulates all the details stemming from the atomic-physics considerations.

As the next step, the system Hamiltonian is rewritten in the interaction picture with respect to the time-independent part H_f (2.7). One obtains the following expression:

$$H_{I2} = \hbar\Omega \begin{pmatrix} 0 & e^{it\omega}\cos\left(\omega_M t + \theta\right) \\ e^{-it\omega}\cos\left(\omega_M t + \theta\right) & 0 \end{pmatrix} \quad , \qquad \omega = \omega_u - \omega_d \tag{2.10}$$

At this point, the Rotating wave approximation (RWA) is introduced. Expanding the $\cos\left(\omega_M t + \theta\right)$ terms as complex exponentials, it will be found that two rotation frequencies emerge in the Hamiltonian H_{I2}: $\omega+\omega_M$ and $\omega-\omega_M$ (as well as their opposite signs). The RWA amounts to neglecting the $\omega + \omega_M$ oscillation frequency as significantly faster than the other frequency (Gerry and Knight [2005]). In other words, the $\omega + \omega_M$ contributions are crossed out. This step implicitly relies on the laser frequency being close to the spacing of the energy levels:

$$\omega \approx \omega_M. \tag{2.11}$$

Introducing the detuning (see Figure 2.1):

$$\Delta = \omega - \omega_M \tag{2.12}$$

the following interaction Hamiltonian is recovered after the RWA:

$$H_{I2-RWA} = \frac{\hbar\Omega}{2} \begin{pmatrix} 0 & e^{it\omega - i\omega_M t - i\theta} \\ e^{-it\omega + i\omega_M t + i\theta} & 0 \end{pmatrix} =$$

$$\frac{\hbar\Omega}{2} \begin{pmatrix} 0 & e^{i\Delta t - i\theta} \\ e^{-i\Delta t + i\theta} & 0 \end{pmatrix}. \tag{2.13}$$

2.1.3 Stark shift

Finally, we derive a standard result for two-level systems, using (2.13), which holds under the following further assumption:

$$\Delta \gg \Omega. \tag{2.14}$$

Setting $\theta = 0$ in (2.13) for clarity and moving to the rotating frame defined by:

$$|\Psi\rangle = \mathrm{Exp}\left[it \begin{pmatrix} -\Delta & 0 \\ 0 & 0 \end{pmatrix}\right] \cdot |\Psi_{old}\rangle \tag{2.15}$$

one recovers the transformed Hamiltonian (Allen and Eberly [1987]):

$$H = \hbar \begin{pmatrix} \Delta & \frac{\Omega}{2} \\ \frac{\Omega}{2} & 0 \end{pmatrix}. \tag{2.16}$$

Now the approximation (2.14) is employed. In the case of small Ω relative to Δ, the matrix (2.16) is approximately diagonal with eigenvectors $\begin{pmatrix} 1 \\ 0 \end{pmatrix}$, $\begin{pmatrix} 0 \\ 1 \end{pmatrix}$ and eigenvalues $\{\Delta, 0\}$. Using this, and writing instead the eigenvalues of (2.16), expanded up to the order Ω^2/Δ^2, one obtains:

$$H \approx \hbar \begin{pmatrix} \Delta + \frac{\Omega^2}{4\Delta} & 0 \\ 0 & -\frac{\Omega^2}{4\Delta} \end{pmatrix}. \tag{2.17}$$

Finally, accounting for Δ in (2.17) by means of a further interaction picture, one derives:

$$H_{SS} = \frac{\hbar\Omega^2}{4\Delta} \begin{pmatrix} 1 & 0 \\ 0 & -1 \end{pmatrix}. \tag{2.18}$$

This effect, whereby a slight change in the energies of the two original levels is recovered, is known as 'Stark shift' (or 'A.C. Stark shift'). Mathematically, it can also be derived using the Dyson series expansion (section 2.2) or the time-averaging approximation techniques developed by James and Jerke [2007]. Corrections to the Hamiltonian (2.18) of the order Ω^3/Δ^2 can

also be obtained.

2.2 The Dyson expansion and secular terms

The Dyson series expansion (Cohen-Tannoudji et al. [2006]) provides a general technique for deriving the effective evolution of a quantum system by means of a series expansion. This is particularly useful for Hamiltonians that contain small terms and fast oscillations.

We define the time-evolution operator for an arbitrary initial quantum state, which propagates the system forward in time from $t = 0$:

$$\Psi(t) = U(t) \cdot \Psi(0) \tag{2.19}$$

Using the time-dependent Schrödinger equation (TDSE) and the arbitrariness of the initial state, one finds that $U(t)$ and the system Hamiltonian $H(t)$ are linked via:

$$\dot{U}(t) = \frac{-i}{\hbar} H(t) \cdot U(t) \tag{2.20}$$

For consistency, one also requires:

$$U(0) = 1 \tag{2.21}$$

In the case where $H(t) = 0$, no time evolution will take place and $U(t)$ will remain constant at 1. In the cases where H(t) is small or undergoing fast oscillations, corrections to $U(t) \approx 1$ can be worked out in a systematic manner: a power series for $U(t)$ can be written down, which is expected to converge in such circumstances.

Integrating (2.20) from 0 to t and adding 1 to ensure (2.21):

$$U(t) = 1 - \frac{i}{\hbar} \int_0^t H(t')U(t')dt' \tag{2.22}$$

This expression can be used to approximate $U(t)$, given $H(t)$, to arbitrary orders in H - the Dyson series. In particular, expanding to the second order

in H:

$$U(t) \approx 1 - \frac{i}{\hbar}\int_0^t H(t')dt' - \frac{1}{\hbar^2}\int_0^t \int_0^{t'} H(t')H(t'')dt''dt' \tag{2.23}$$

Here, the convention in the double integral is to perform the innermost integral first. Applying (2.22) repeatedly enables the continuation of the series to arbitrary orders. A prominent deviation from $U(t) \approx 1$ could amount to finding a constant term of significant magnitude after performing the integrals in (2.23), or possibly recovering a term that grows linearly with t. Such a term is referred to as a secular term.

Finding a secular term $U_s(t) = qt$ in the right hand side of (2.23) has a simple interpretation in modifying the approximation $H(t) \approx 0$, under a set of simplifying conditions: integrating the TDSE for a constant Hamiltonian

$$U(t) = e^{-iHt/\hbar} \tag{2.24}$$

and expanding for the case of short times:

$$U(t) \approx 1 - iHt/\hbar \tag{2.25}$$

Comparison with (2.23) reveals that the secular term qt can be interpreted in such circumstances as a constant non-zero effective Hamiltonian:

$$H \approx i\hbar q \tag{2.26}$$

A more detailed analysis reveals that (2.26) also holds under more general circumstances (Cohen-Tannoudji et al. [2006]).

2.3 Quantum adiabatic theorem and the Berry's phase

The Quantum adiabatic theorem (Cohen-Tannoudji et al. [2006]) states that for a system that is governed by a Hamiltonian, which is varying slowly in time, compared to the state energy separation, any initial energy eigenstate will be preserved as the corresponding eigenstate of the

evolving Hamiltonian during the time evolution, allowing for no transitions or exchange of energy to take place. In other words, any population in an eigenstate of the system at the beginning of the time evolution will be transformed to the corresponding energy eigenstate at any subsequent times. The criterion for maintaining this property of adiabacity is given by Aharonov and Anandan [1987]:

$$\sum_{i \neq j} \left| \frac{\hbar \langle \Psi_i | \dot{H} | \Psi_j \rangle}{(E_i - E_j)^2} \right| \ll 1 \tag{2.27}$$

with the variable definitions provided below in the text.

For the adiabatic state evolution, there will also be a phase factor acquired by the population within the state - the Berry's phase - which is now derived (Rohrlich [2007]; Vedral [2003]). The derivation amounts to substituting a trial solution into the TDSE. The Hamiltonian is specified to depend on a set of parameters R_i that themselves depend on time: $H(\mathbf{R}(t))$. The i'th energy eigenstate is given by:

$$H|\Psi_i\rangle = E_i|\Psi_i\rangle \tag{2.28}$$

The system is assumed to occupy this eigenstate initially. Furthermore, given the adiabacity condition, no transitions to other eigenstates will occur during the time evolution, so that (2.28) is taken to hold for all times (here assuming $E_i(t)$ and a time-dependent state vector).

Berry phase is obtained for the particular eigenstate by employing the trial solution: $|\Psi_i\rangle e^{i\phi_i}$. Substitution into the TDSE gives:

$$\begin{aligned} i\hbar\partial_t \Big(|\Psi_i\rangle e^{i\phi_i} \Big) &= H \Big(|\Psi_i\rangle e^{i\phi_i} \Big) \\ i\hbar \Big(i\dot{\phi}_i |\Psi_i\rangle + |\dot{\Psi}_i\rangle \Big) &= E_i |\Psi_i\rangle \end{aligned} \tag{2.29}$$

Here, the second line follows from using the adiabatic condition (2.28) on the right hand side and canceling the exponential factors. Further manip-

ulation yields:

$$\dot{\phi}_i = i\langle\Psi_i||\dot{\Psi}_i\rangle - \frac{1}{\hbar}E_i \tag{2.30}$$

The second term provides the usual dynamical phase associated with the energy of the system. In the cases to be discussed in further chapters, E_i will be set to zero and therefore not relevant. Re-expressing the time derivative in the remaining term and integrating, one finds the sought-after expression for the Berry phase:

$$\begin{aligned} \dot{\phi}_i &= i\langle\Psi_i|\nabla_{\mathbf{R}}|\Psi_i\rangle \cdot \frac{d\mathbf{R}}{dt} \\ \Phi_i &= i\int_{\mathbf{R}_{in}}^{\mathbf{R}_f} \langle\Psi_i|\nabla_{\mathbf{R}}|\Psi_i\rangle \cdot d\mathbf{R} \end{aligned} \tag{2.31}$$

Taking the initial system state to be $|\Psi_i(t_{in})\rangle$, equation (2.31) provides the Berry phase factor acquired in traversing the path $\mathbf{R}(t)$, so that the final state at the end of the path (assuming zero dynamical phase) is $|\Psi_i(t_f)\rangle e^{i\Phi_i}$. Expression (2.31) is the one employed in the calculations of later chapters.

2.4 Energy level structure of $^{171}Yb^+$

As the principal physical system for experimental implementation of the quantum techniques discussed in later chapters, we introduce and briefly describe the ionised $^{171}Yb^+$ atom. Its simple energy-level structure makes it a natural candidate from the experimental point of view (Wang et al. [2011]). In particular, the single outer $n = 6, l = 0$ electron occupies an otherwise empty electron shell, with the two next-lowest $n = 5, l = \{0, 1\}$ levels being fully occupied. Further, all the other shells characterised by $n = \{1..4\}$ are fully closed in the electron configuration.

Therefore, a simple hydrogen-like energy level structure is found for the outer electron. In addition, the spin for the $^{171}Yb^+$ nucleus is found to be 1/2, making also the hyperfine splitting particularly simple.

Figure 2.2 plots the lowest-lying hyperfine-split energy levels of the single outermost electron in the presence of a constant positive magnetic field. Standard spectroscopic notation is employed. This represents the typical

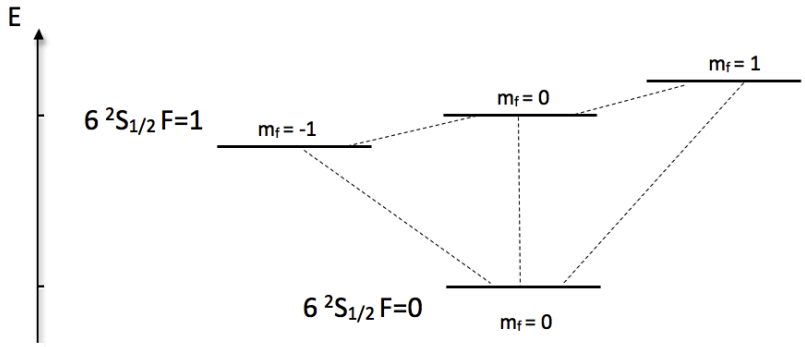

Figure 2.2: Energy-level diagram and quantum numbers for the hyperfine-split ground state of $^{171}Yb^{+}$. Allowed transitions are indicated by dashed lines. A constant positive B-field is assumed.

experimental set-up for the implementation of STIRAP and quantum gate processes discussed in further chapters. Allowed transitions are indicated by dashed lines.

The study by Blatt et al. [1983] presents a detailed energy-level diagram for this system as well as provides an accurate measurement of the singlet-triplet energy splitting in the absence of ambient magnetic field, which is approximately $A = 2\pi \cdot 12.6$ GHz. The $m_f = \pm 1$ states respond exactly linearly to external magnetic field B, with the change in energy given by:

$$\Delta E = \pm g_F \mu_B m_f B = \pm \mu_B B \tag{2.32}$$

The response of the two $m_f = 0$ levels can be approximated to the lowest order (Foot [2004]) by:

$$\Delta E = \pm \frac{(\mu_B B)^2}{A}. \tag{2.33}$$

Here, μ_B is the Bohr magneton.

2.5 Stimulated Raman adiabatic passage

This section presents a standard technique for selective adiabatic population transfer: Stimulated Raman adiabatic passage (STIRAP) will be invoked as an auxiliary experimental technique in chapters 6, 7, which dis-

cuss quantum gate implementation. It will also be discussed briefly in its own right in chapter 3.

Discovered and experimentally used since around the early 1990's (Gaubatz et al. [1990]; He et al. [1990]; Kuklinski et al. [1989]), STIRAP has a number of desirable properties as a transfer method. The transfer process is efficient and relatively insensitive to the detailed shape of the laser pulses, due to the intrinsic use of adiabatic following. Because STIRAP involves an intermediate state, the transfers can be accomplished even between levels where direct transitions would be forbidden. Moreover, possible spontaneous emission from the intermediate state leaves no effect on the transfer process (Bergmann et al. [1998]), as will be demonstrated.

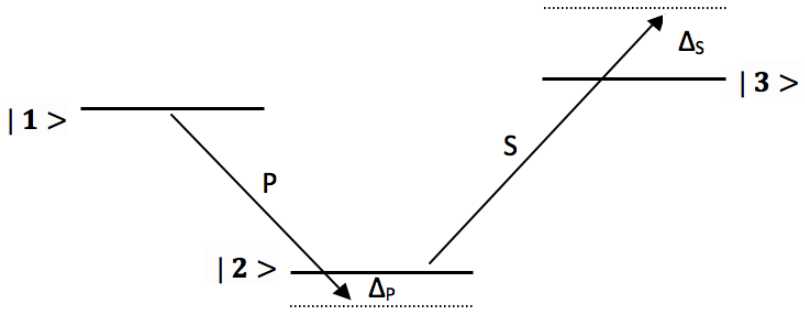

Figure 2.3: Arrangement for the STIRAP process, with two couplings ('Pump' and 'Stokes') and detunings indicated. Transfer from $|1\rangle$ to $|3\rangle$ is accomplished by adiabatic following.

Figure 2.3 presents the 3-level arrangement to be employed. It is desired to transfer population, all initially residing in state $|1\rangle$, reliably onto state $|3\rangle$. Two laser pulses are employed, and an essential use will be made of adiabatic following (although the Berry's phase will not be discussed here, because of interest in population transfer only). It will be shown how state $|2\rangle$, though essential for the process, is never populated during the transfer.

2.5.1 Hamiltonian

Two sinusoidal laser pulses of Rabi frequencies $\Omega_{S,P}(t)$ and detunings $\Delta_{S,P}$ are employed. We assume zero laser phases for the simplified case presented. In direct analogy to (2.13), the Hamiltonian for the three-state

system specified in Figure 2.3 can be written down in the interaction picture with respect to energy level height, after performing the RWA:

$$H_{RWA} = \frac{\hbar}{2} \cdot \begin{array}{c} \\ |1\rangle \\ |2\rangle \\ |3\rangle \end{array} \begin{array}{c} \begin{array}{ccc} \langle 1| & \langle 2| & \langle 3| \end{array} \\ \begin{pmatrix} 0 & \Omega_P e^{-i\Delta_P t} & 0 \\ \Omega_P e^{i\Delta_P t} & 0 & \Omega_S e^{i\Delta_S t} \\ 0 & \Omega_S e^{-i\Delta_S t} & 0 \end{pmatrix} \end{array}. \tag{2.34}$$

As the next step, one transforms to the rotating frame defined by:

$$|\Psi\rangle = \mathrm{Exp}\left[it \begin{pmatrix} 0 & 0 & 0 \\ 0 & -\Delta_P & 0 \\ 0 & 0 & \Delta_S - \Delta_P \end{pmatrix} \right] \cdot |\Psi_{old}\rangle \tag{2.35}$$

Making the appropriate transformation (Allen and Eberly [1987]), the Hamiltonian becomes:

$$H = \frac{\hbar}{2} \begin{pmatrix} 0 & \Omega_P & 0 \\ \Omega_P & 2\Delta_P & \Omega_S \\ 0 & \Omega_S & 2(\Delta_P - \Delta_S). \end{pmatrix}. \tag{2.36}$$

Specifying, further, that the two detunings are equal (see Figure 2.3):

$$\Delta_P = \Delta_S \tag{2.37}$$

one arrives at the standard Hamiltonian quoted in the STIRAP literature (Bergmann et al. [1998]; Fewell et al. [1997]; Vitanov et al. [2001]):

$$H = \frac{\hbar}{2} \begin{pmatrix} 0 & \Omega_P(t) & 0 \\ \Omega_P(t) & 2\Delta_P & \Omega_S(t) \\ 0 & \Omega_S(t) & 0 \end{pmatrix} \tag{2.38}$$

2.5.2 Population transfer

STIRAP relies on the zero-eigenvalue eigenstate of the Hamiltonian (2.38), which is a mixture of $|1\rangle$ and $|3\rangle$:

$$\begin{aligned} |\Phi_0\rangle &= \cos\theta|1\rangle - \sin\theta|3\rangle \\ \theta(t) &= \tan^{-1}\left(\frac{\Omega_p(t)}{\Omega_s(t)}\right). \end{aligned} \tag{2.39}$$

By the adiabatic approximation, a system initialised in $|\Phi_0\rangle$ will remain in that state provided the Hamiltonian is varied slowly enough. It is seen that the mixing angle characterising $|\Phi_0\rangle$ changes with the Rabi frequencies, with the available range spanning from $\theta = 0$ to $\theta = \pi/2$. Therefore, by choosing an appropriate pulse sequence, one can achieve an effective adiabatic rotation of the composition of $|\Phi_0\rangle$ from $|1\rangle$ to $|3\rangle$. In other words, the desired population transfer would be achieved.

For this goal, a pulse sequence is required such that:

$$\begin{aligned} &(\Omega_p/\Omega_s)|_{t\to-\infty} \to 0, \\ &(\Omega_p/\Omega_s)|_{t\to+\infty} \to \infty \end{aligned} \tag{2.40}$$

and the variation is slow enough that the adiabacity condition is satisfied. Figure 2.4 (top left) shows such a pulse sequence, with the correct asymptotic behaviour. It is typical for STIRAP experiments to employ a pair of delayed Gaussian pulses. Somewhat counter-intuitively, Stokes pulse must precede the Pump pulse in the successful STIRAP procedure.

Figure 2.4 (top right) illustrates the population transfer by plotting the time evolution of the squared amplitudes for $|1\rangle$ and $|3\rangle$, calculated using (2.39) for a pair of delayed Gaussian pulses. Even though state $|2\rangle$ is crucial for the process, it is never populated during the pulse sequence. Figure 2.4 (bottom) also plots the time evolution of the eigenvalues of H. It can be deduced from the Hamiltonian (2.38) that states $|1\rangle$ and $|3\rangle$ have zero eigenvalues at the beginning/end of the pulse sequence and form a degenerate pair. The degeneracy is lifted, as the pulse sequence proceeds. We have labeled the adiabatic state $|\Phi_0\rangle$ (2.39), which retains the zero eigenvalue during the pulse sequence. Moreover, the energy of the third

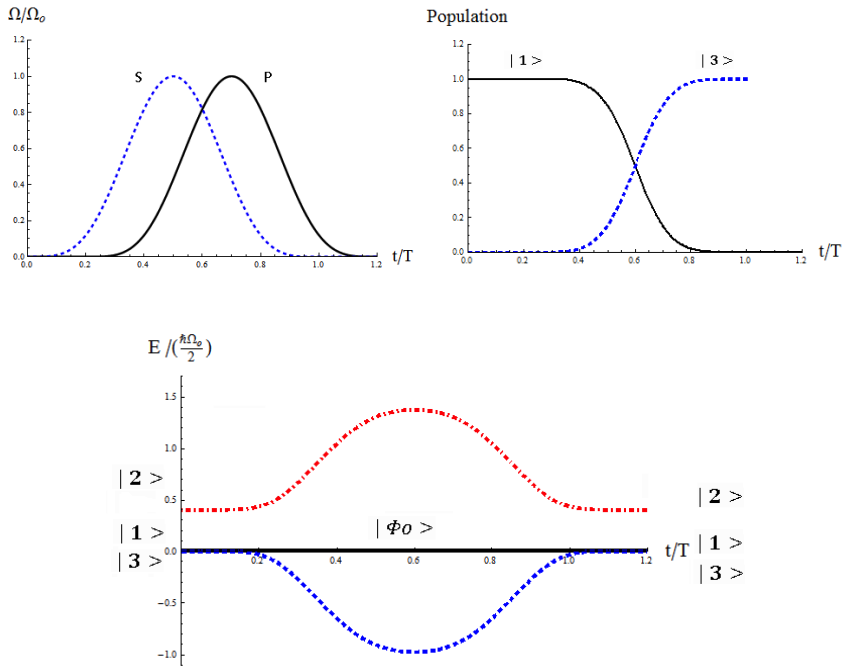

Figure 2.4: STIRAP pulses and population transfer (plotted in dimensionless units). Top left: the Gaussian pulse sequence showing the Rabi frequencies of the Pump and the Stokes fields. Top right: evolution in time of the squared amplitudes of components $|1\rangle$ and $|3\rangle$, obtained using (2.39) and the pair of Gaussian pulses. Bottom: time evolution of the eigenvalues of the STIRAP Hamiltonian (2.38). Eigenstate $|\Phi_0\rangle$ is identified throughout the pulse sequence, and all three states are also labeled at the beginning/end of the pulses. The single detuning is set to $\Delta_P/\Omega_0 = 0.2$.

state, $|2\rangle$, at the beginning and end of the pulse sequence is also fixed by the Hamiltonian (2.38).

A crucial condition for the existence of the state $|\Phi_0\rangle$ is the requirement $\Delta_P = \Delta_S$ to yield the Hamiltonian (2.37). This is a condition unlikely to be fulfilled at all times in realistic laboratory conditions, due to magnetic noise affecting level energies. This point will be investigated further in chapter 3.

Chapter 3

STIRAP in the presence of magnetic noise

A central theme of the present dissertation is the task of coping with the effects of magnetic noise in realistic laboratory conditions. As will be argued in the later chapters, the usage of long-wavelength radiation for quantum computing necessitates, within the design considered, the usage of magnetic-sensitive states for encoding of quantum information. Hence, techniques will need to be developed to achieve shielding against this source of noise, and we will consider in particular the usage of dressed states as a fruitful shielding strategy.

This chapter explores the role of magnetic noise in STIRAP, showing that low-amplitude noise effects are expected to cause a negligible disturbance, albeit a breakdown of the process of adiabatic following would be involved. This discussion is added in order to present the workings of STIRAP in a more realistic context, and also since STIRAP plays an intrinsic role in the quantum gate designs presented in further chapters.

The original content of this chapter amounts to discussing known results from previous work in the context of a novel research question.

3.1 The role of two-photon detuning

Continuing from section 2.5, the following definition is introduced:

$$\Delta_3 = \Delta_P - \Delta_S. \tag{3.1}$$

So that the STIRAP Hamiltonian can be written as (see (2.36)):

$$H = \frac{\hbar}{2} \begin{pmatrix} 0 & \Omega_P & 0 \\ \Omega_P & 2\Delta_P & \Omega_S \\ 0 & \Omega_S & 2\Delta_3 \end{pmatrix}. \tag{3.2}$$

As presented previously, STIRAP relies on the requirement $\Delta_3 = 0$ (2.37), in order for there to exist the zero-eigenvalue adiabatic state, which is used in the population transfer. This condition can normally be met by setting experimentally the appropriate detunings, however this becomes problematic when magnetic-sensitive states are being used.

We consider the STIRAP arrangement presented in Figure 2.3, as applied to trapped $^{171}Yb^{+}$ ions (Figure 2.2), a design where two magnetic-sensitive levels are involved. A deviation μ in the energy level height due to a deviation in the surrounding static magnetic field will introduce the following variation in the detunings:

$$\begin{aligned} \Delta_P &\rightarrow \Delta_P + \mu \\ \Delta_3 &\rightarrow \Delta_3 + 2\mu \end{aligned} \tag{3.3}$$

thus upsetting the $\Delta_3 = 0$ requirement. It is of interest to discuss how the STIRAP transfer can still be accomplished with the help of a non-adiabatic effect. This has been discussed extensively by Fewell et al. [1997]. We review these arguments, which would apply for the case of constant μ (3.3). We then comment briefly on the case where μ is understood as a time-dependent stochastic process.

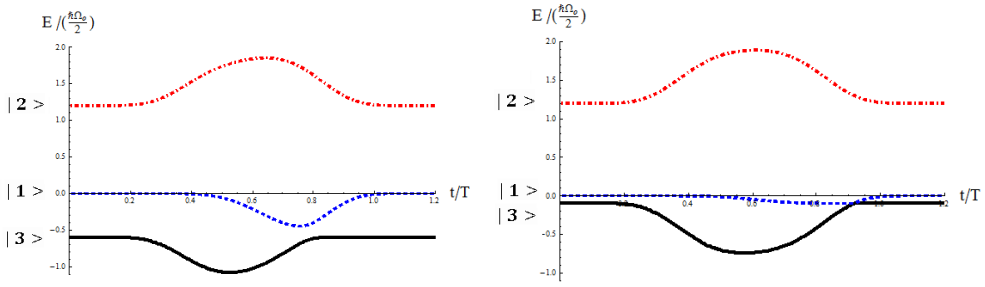

Figure 3.1: STIRAP with two-photon detuning, illustrated by time evolution of the energy eigenvalues. As in Figure 2.4, Gaussian pulses and dimensionless units are used. Left: $\Delta_P/\Omega_0 = 0.6$, $\Delta_3/\Omega_0 = -0.3$. Right: $\Delta_P/\Omega_0 = 0.6$, $\Delta_3/\Omega_0 = -0.05$. The width of the avoided crossing present in both cases is seen to decrease with Δ_3/Ω_0.

3.2 Transition probability in the static case

The effect that enables successful STIRAP even for $\Delta_3 \neq 0$ is non-adiabatic transitions, or 'jumps'. Following the adiabatic theorem (section 2.3), no transitions across energy eigenstates will ever occur, provided that the Hamiltonian is varied slowly enough. However, this will be violated in the instances where the evolution occurs faster than the required 'slow' rate, so that transitions would indeed become possible. A simple linearised model for such non-adiabatic transitions across energy levels has been developed: the Landau-Zener model (Landau and Lifshitz [1981]; Zener [1932]). This provides a concise formula for the probability of an occurence of a non-adiabatic jump, showing that it approaches 1 for small energy gaps and fast rate of variation in the Hamiltonian.

Figure 3.1 plots the evolution of eigenvalues during the STIRAP sequence with non-zero Δ_3 set to two values. Again, the states can be unambiguously identified and labeled at the beginning and end of the pulse sequence. In contrast to Figure 2.4, where the presence of a zero-eigenvalue state throughout the sequence is clearly seen, no such state is present in the $\Delta_3 \neq 0$ case. From the Hamiltonian (3.2), it is also clear that states $|1\rangle$, $|2\rangle$ and $|3\rangle$ will return to their original eigenvalues at the end of the pulse sequence, so that no crossing of energy levels has taken place. By adiabatic evolution alone, no transit from $|1\rangle$ to $|3\rangle$ would thus be possible.

However, such transit would be enabled by a jump over the avoided

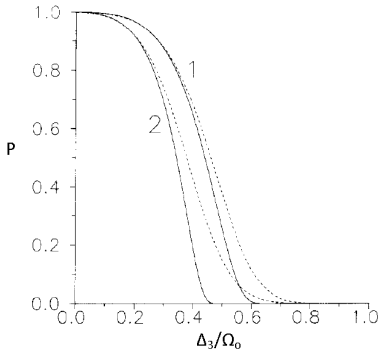

Figure 3.2: Probability of a successful STIRAP process, as dependent on Δ_3 (Danileiko et al. [1994]). Landau-Zener calculation results (solid) are plotted alongside simulation results (dashed). The graphs represent cases with $\Delta_P/\Omega_0 = 0$ (labeled 1) and $\Delta_P/\Omega_0 = 0.5$ (labeled 2). The other parameters are $\Omega_0 \cdot w = 40, d = w/2$. Here, d is the pulse delay and w is the Gaussian pulse width.

crossing, which is seen to be present in Figure 3.1. It is also seen that the crossing becomes increasingly sharp as Δ_3 is reduced, suggesting an increased transfer probability. This non-adiabatic jump process provides the transfer mechanism between STIRAP using $\Delta_3 = 0$ and small deviations from this condition, whereby successful transfer with high probability would still be expected (Fewell et al. [1997]).

Considering (3.3) and Figure 3.1, one also concludes that the deviation in Δ_P due to magnetic noise amounts to a much less significant effect, since the state $|2\rangle$, whose height is governed by Δ_P, is not participating in the non-adiabatic transition. However, this conclusion would no longer hold in more complex arrangements of detunings, where possibly two non-adiabatic transitions become necessary. Such cases are discussed by Fewell et al. [1997].

As mentioned, the probability of successful transit over an avoided crossing can be calculated, in the first approximation, using the Landau-Zener model, which provides the standard point of departure beyond the adiabatic theorem. The Landau-Zener model assumes a linear crossing, taking the evolution time to infinity both before and after the crossing point. The model has been applied to STIRAP by Danileiko et al. [1994], and Figure 3.2 plots the probability for a successful STIRAP transfer (which in

this case implies a successful non-adiabatic transition) for two instances of $\Delta_3 \neq 0$.

Results for the Landau-Zener calculation (solid) are plotted in Figure 3.2 together with numerical simulations of the TDSE (dashed). It is seen that good agreement between the Landau-Zener model and the simulation results is obtained. The absence of perfect agreement can be explained by the violation of the assumptions of the Landau-Zener derivation. Importantly, it is also seen that for sufficiently small Δ_3/Ω_0, the probability for successful STIRAP approaches unity. Judging from Figure 3.2, a successful STIRAP sequence with nonzero Δ_3 would be possible with near-perfect rate of success, provided $\Delta_3/\Omega_0 \leq 0.1$, even after the magnetic effects have been taken into account.

In summary, arguments based on static deviations only suggest that reliable STIRAP is enabled even for $\Delta_3 \neq 0$, which will inevitably be the case in a noisy environment, with non-adiabatic transitions playing an instrumental role.

3.3 Considering stochastic effects

It is difficult to give a concise analytical treatment for the behaviour of non-adiabatic transfer processes in the presence of time-dependent stochastic noise. The possibility of several transitions during a single sweep needs to be considered, and the problem is complicated further by the stochastic nature of noise.

The Landau-Zener model can be extended to introduce effects of noise (Kayanuma [1984]; Pokrovsky and Sinitsyn [2003]). However, numerical simulation with a particular set of experimental parameters would probably be the most fruitful approach. Recent experimental work (Timoney [2010]) demonstrates 95% STIRAP success probability, using magnetic-sensitive states of $^{171}Yb^{+}$ in noisy laboratory conditions, for the two-photon detuning set in the range of $-0.1 < \Delta_3/\Omega_0 < 0.1$. The experiment used $\Delta_P = 0$, $\Omega_0 = 2\pi \cdot 17.5$ kHz. We consider a spectral measurement of noise by the same experimental group in section 6.6 to quantify its magnitude. The term $\mu(t)$ is thus found to have an estimated standard deviation of $2\pi \cdot 88$ Hz, suggesting the noise to be small in amplitude compared to Ω_0.

Chapter 4

Notation summary

This chapter presents unified notation for the remainder of the dissertation as a useful reference. There is no other new material included.

4.1 General definitions

$\hbar = 1$ set for the remainder of the dissertation for clarity of presentation

$b^\dagger, b$ – phonon operators for a shared motional mode, later redefined as:

$$\tilde{b}^\dagger = e^{i\nu t} b^\dagger \ , \ \tilde{b} = e^{-i\nu t} b$$

ν – energy spacing of the motional mode

n – phonon number for the motional mode

m – mass of the trapped ion

z – displacement along trap axis relative to the particle's equilibrium position

N – particle number (4.1)

We also define ζ, which is a prefactor linking axial displacement z and the sum of phonon operators (see e.g. (5.3)). ζ is equal to $1/\sqrt{2}$ for the two-particle case, both for the centre-of-mass and the breathing modes. For the N-particle case, $\zeta = 1/\sqrt{N}$ for the centre-of-mass mode and ζ is close to $1/\sqrt{N}$ for the other modes (Šašura and Bužek [2002]).

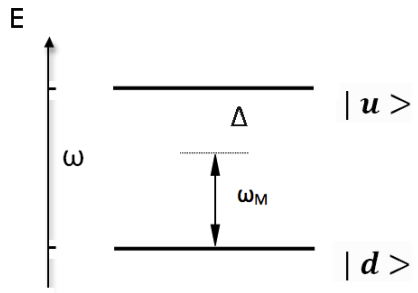

Figure 4.1: Generic two-level system with laser addressing.

4.2 Definitions pertaining to the two-level system

We restate some of the definitions used in section 2.1 as well as introduce new ones. Figure 4.1 provides the illustration.

H_M – the dipole interaction Hamiltonian due to the light field

ω – energy spacing of the two-level system, we also use

ω_0 for position-dependent $\omega(z)$ to refer to the ion's equilibrium position

Ω – Rabi frequency of the light field

ω_M – frequency of the light field

k – wave number of the light field

$\Delta = \omega - \omega_M$ – light field detuning, we also use $\Delta = \omega_0 - \omega_M$

$\eta = \zeta k \sqrt{\frac{1}{2m\nu}}$ – definition of the conventional Lamb-Dicke parameter

$\varepsilon_c = \partial_z \omega(z) \cdot \zeta \sqrt{\frac{1}{2m\nu}} \cdot \frac{1}{\nu}$ – parameter definition

$\gamma = \tan^{-1}\left(\frac{\varepsilon_c}{\eta}\right) \cdot \frac{\omega_0}{\nu}$ – parameter definition

$\eta' = \sqrt{\varepsilon_c^2 + \eta^2}$ – effective Lamb-Dicke parameter

$\sigma_z = |u\rangle\langle u| - |d\rangle\langle d|$

$\sigma_+ = |u\rangle\langle d| \quad , \quad \sigma_- = |d\rangle\langle u|.$ (4.2)

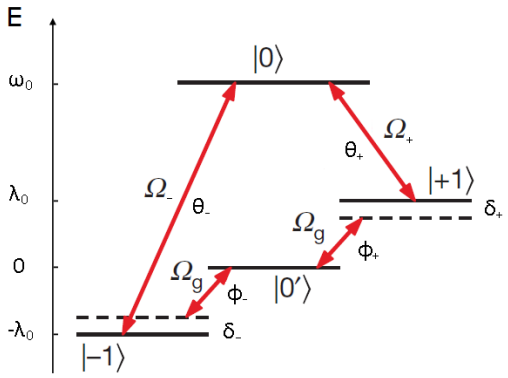

Figure 4.2: Four-level system for the realisation of the dressed state qubit and single-qubit gates, together with couplings in the microwave and radio wave domain ($\Omega_{+/-}$ and Ω_g respectively). Rabi frequencies are denoted by Ω_i, detunings by δ_i and laser phases by θ_i, ϕ_i. Another possible coupling is between $|0\rangle$ and $|0'\rangle$, which is described using Ω_z, θ_z and δ_z. $|-1\rangle$ and $|1\rangle$ are the magnetic-sensitive levels, and the presence of a positive magnetic field is assumed.

4.3 Definitions for the dressed-state design

Figure 4.2 gives the definitions of the energy levels and the addressing fields for the system considered. The qubit is to be realised using either $\{|D\rangle, |0'\rangle\}$ or $\{|B\rangle, |0'\rangle\}$ as the logical states. We introduce the definitions:

$$|D\rangle = \frac{1}{\sqrt{2}}(|-1\rangle - |1\rangle)$$
$$|B\rangle = \frac{1}{\sqrt{2}}(|-1\rangle + |1\rangle). \tag{4.3}$$

For the D-qubit:	For the B-qubit:
$\|u\rangle = \frac{1}{\sqrt{2}}(\|B\rangle + \|0\rangle)$	$\|u\rangle = \frac{1}{\sqrt{2}}(\|D\rangle + \|0\rangle)$
$\|d\rangle = \frac{1}{\sqrt{2}}(\|B\rangle - \|0\rangle)$	$\|d\rangle = \frac{1}{\sqrt{2}}(\|D\rangle - \|0\rangle)$

(4.4)

μ – energy deviation of level $|1\rangle$ ($-\mu$ for $|-1\rangle$) due to magnetic noise

$\delta_\Omega = \Omega_- - \Omega_+$ – noise term due to microwave Rabi frequency fluctuation

f – Gaussian noise in $\Omega_{+/-}$ is added with standard deviation $f\Omega$ (4.5)

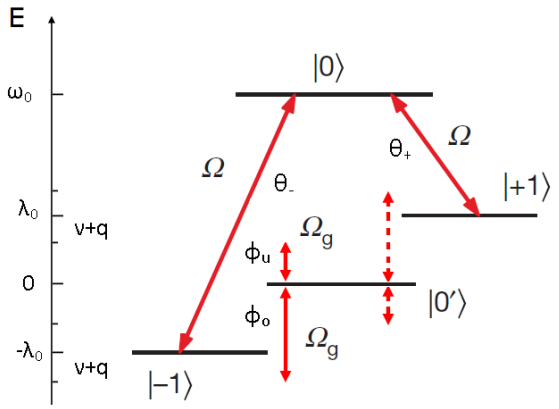

Figure 4.3: Realising the two-qubit entangling gate with the help of a magnetic gradient. Two radio frequency fields (Rabi frequency Ω_g), detuned by $\pm q$ from the motional sidebands, generate four couplings between $|-1\rangle$, $|0'\rangle$, and $|1\rangle$. Microwave fields (Rabi frequency Ω) contribute to the shielding. The $|-1\rangle$, $|1\rangle$ states are linearly dependent on magnetic field, so the presence of a positive magnetic gradient makes their energy position-dependent. λ_0 denotes $\lambda(z)$ at the ion's equilibrium position.

4.4 Definitions pertaining to the dressed-state entangling gate

Figure 4.3 provides the experimental arrangement. The gate will be illustrated for the case of the D-qubit. The following additional variables are introduced:

q – sideband detuning of the RF fields (see Figure 4.3)

R – integer parameter characterising the fast
Mølmer-Sørensen gate (see (7.18))

$\tilde{\sigma}_z = |1\rangle\langle 1| - |-1\rangle\langle -1|$

$\tilde{\sigma}_+ = |D\rangle\langle 0'| \quad , \quad \tilde{\sigma}_- = |0'\rangle\langle D|$

$\kappa = \partial_z(\lambda(z))\dfrac{\zeta}{\sqrt{2m\nu}}$ – parameter definition, Figure 4.3 defines $\lambda(z)$.

(4.6)

We also define:

$$\tilde{\eta} = \kappa/\nu. \tag{4.7}$$

In the case where interactions are created by microwave and radio wave light and the conventional Lamb-Dicke parameter is essentially zero, $\tilde{\eta}$ can be thought of as the effective Lamb-Dicke parameter. For clarity of presentation, this definition differs by a factor 1/2 from the definition in section 4.2, where η' is introduced.

Chapter 5

Introducing the dressed-state scheme

This chapter introduces in detail the physical set-up for realising quantum computation using microwave-dressed states. Motivation for the usage of a magnetic gradient and the dressed states is provided, using explicit Hamiltonians and derivations. Moreover, a detailed description of the experimental set-up used throughout the following chapters is also given.

To summarise the argument, there is strong interest in the deployment of long-wavelength sources in trapped-ion quantum information processing, because of the considerable experimental advantages that such a change would bring. However, there are two issues, tackled easily in the traditional laser-based approach, which need to be solved if the long-wavelength design is to succeed. Firstly, there is the issue of individual addressing of the trapped particles. Laser beams can be tightly focused in physical space while microwaves cannot. Secondly, the conventional Lamb-Dicke parameter, which governs the strength of atom-motional mode interactions, is too small in the long-wavelength design to yield useful gate operations. It will be shown how both of these issues are solved by the addition of static magnetic gradient along the trap axis, and detailed calculations will be employed in this chapter to illustrate the point. The usage of dressed states is motivated by the need to shield the system against magnetic noise. The magnetic-gradient approach necessitates the use of magnetic-sensitive states for the logical qubit, thus exposing the system to magnetic noise and

the resulting decoherence effects. The usage of dressed states is employed as an effective shielding technique. The proposal will be outlined in this chapter, and gates designed in this approach will be presented in further chapters, demonstrating the shielding effect both mathematically and in simulation.

Concerning the material of this chapter, section 5.2 is a summary of previous theoretical work, sections 5.1 and 5.3 provide original discussion of known results and considerations, section 5.4 provides an original derivation, retracing the steps from a known paper more explicitly and correcting ambiguities. Sections 5.5 and 5.6 provide original discussion of previously published results.

5.1 Motivation for the long-wavelength approach

The starting point for the research endeavor pursued in the present thesis is the desire to use long-wavelength radiation for the realisation of quantum gates. Numerous experimental difficulties can be pointed out for the usage of laser light in quantum information processing, such as the requirement for tight beam focusing and difficult constraints on the laser stability (Mintert and Wunderlich [2001, 2003]). The laser set-ups tend to occupy considerable amount of space and involve complex laboratory arrangements, making them hard to miniaturise. There is considerable effort involved in the installation and callibration of the equipment. Further laboratory work is needed to reduce drifts and achieve the necessary standards of stability and other characteristics required for quantum information processing.

In contrast, microwave and radio wave sources have long been studied and developed, and represent a mature technology. Cheap off-the-shelf components are available for the experimental realisation and well-developed techniques exist for the callibration and attainment of the neccesary beam properties. This would represent a serious advantage in terms of the experimental burden involved. Moreover, long-wavelength sources are also amenable to miniaturisation, so that the prospect of quantum

gates integrated on a chip becomes feasible. In summary, the introduction of long-wavelength sources would amount to a welcome development and serious progress in the field of experimental quantum gate realisation.

5.2 The Hamiltonian for conventional ion-field coupling

First, we briefly summarise the mathematics behind the interaction of a laser field with a chain of trapped ions in the traditional set-up (Cirac et al. [1995]; Gulde [2003]; Riebe [2005]; Rohde [2001]; Roos [2000]). The notation has been specified in (4.1) and (4.2).

We consider a two-level system embedded in an SHO-type motional mode. The free Hamiltonian will be the sum of the atomic and motional parts. After removing the ground-state phonon energy:

$$H = \frac{\omega}{2}\sigma_z + \nu\, b^\dagger b \tag{5.1}$$

Here, the σ_z term corresponds to H_f in (2.7). And the ν term is the typical phonon energy operator.

Interactions between the atomic levels and coherent laser light are modeled within the dipole approximation. This gives an interaction Hamiltonian of the form:

$$H_M = \frac{\Omega}{2}(\sigma_+ + \sigma_-) \cdot (e^{i(\omega_M t - kz)} + h.c.) \tag{5.2}$$

This term corresponds to H_I in (2.7), with the laser phase omitted for clarity of presentation. The wave number k has been included explicitly, because, even though the light field is not expected to show variation across the spatial extent of the atom (the dipole approximation), there is variation to be expected across the spatial extent covered by the vibration of the atom.

The Hamiltonian is further modified using:

$$z = \zeta \sqrt{\frac{1}{2m\nu}} \cdot (b^\dagger + b). \tag{5.3}$$

This is a property linking the phonon operators and the displacement of a particle in an SHO-type motional mode (Šašura and Bužek [2002]). Moreover, one uses:

$$\eta = \zeta k \sqrt{\frac{1}{2m\nu}} \tag{5.4}$$

which is the definition of the conventional Lamb-Dicke parameter η. This enables one to substitute:

$$kz = \eta \cdot (b^\dagger + b) \tag{5.5}$$

in the dipole Hamiltonian.

The full Hamiltonian is given by the sum $H + H_M$. To investigate the effect of H_M on the system, one moves to the interaction picture with respect to H. A lengthy calculation yields:

$$\tilde{H} = \frac{\Omega}{2}\left(\sigma_+ e^{i\eta(\tilde{b}+\tilde{b}^\dagger)} e^{i\Delta t} + \sigma_+ e^{-i\eta(\tilde{b}+\tilde{b}^\dagger)} e^{i(\omega+\omega_M)t} + h.c.\right), \tag{5.6}$$

where $\tilde{H}$ is the dipole Hamiltonian in the interaction picture. And the detuning is introduced following (4.2).

Next, one performs the RWA, which in the present case means canceling the terms oscillating with $\omega_M + \omega$ in favour of the terms oscillating with Δ. This gives:

$$\tilde{H} = \frac{\Omega}{2}\left(\sigma_+ e^{i\eta(\tilde{b}+\tilde{b}^\dagger)} e^{i\Delta t} + h.c.\right). \tag{5.7}$$

Also, the η parameter is assumed to be small ('Lamb-Dicke regime'), enabling one to approximate the relevant exponentials. This yields:

$$\tilde{H} = \frac{\Omega}{2}\left(\sigma_+ [1 + i\eta(be^{-i\nu t} + b^\dagger e^{i\nu t})] e^{i\Delta t} + h.c.\right). \tag{5.8}$$

Hamiltonian (5.8) can be used to carry out the kind of interactions envisaged in Figure 1.1. This is realised by setting appropriate values of Δ. In particular, equation (5.8) is further approximated by fixing Δ and

performing a second RWA to yield:

$$\tilde{H}_c = \frac{\Omega}{2}\left(\sigma_+ + \sigma_-\right) \qquad \Delta = 0 \tag{5.9}$$

$$\tilde{H}_b = \frac{\Omega}{2} i\eta \left(b^\dagger \sigma_+ - b\sigma_-\right) \qquad \Delta = -\nu \tag{5.10}$$

$$\tilde{H}_r = \frac{\Omega}{2} i\eta \left(b\sigma_+ - b^\dagger \sigma_-\right) \qquad \Delta = \nu \tag{5.11}$$

These are the Hamiltonians for the 'carrier', the 'blue sideband' and the 'red sideband'. The two sideband Hamiltonians, containing terms that mix electronic and phonon excitations, are also referred to as representing the Jaynes-Cummings form (Jaynes and Cummings [1963]).

Solving the TDSE with these Hamiltonians, one obtains oscillatory solutions, where the population is seen to transfer between $|d, n\rangle \leftrightarrow |u, n\rangle$ (carrier), $|d, n\rangle \leftrightarrow |u, n+1\rangle$ (red sideband) and $|d, n\rangle \leftrightarrow |u, n-1\rangle$ (blue sideband), where n counts the number of phonons in the mode in question.

An additional degree of freedom not included in the derivation is the laser phase. Once the phase is added in the carrier Hamiltonian (5.9), it is found that any arbitrary single-qubit rotation becomes feasible. In other words, arbitrary rotations on the Bloch sphere representing the qubit state can be realised using an appropriate carrier pulse sequence. Moreover, the two sideband Hamiltonians enable the execution of coupling to the shared motional mode, which is a crucial ingredient for the implementation of a multi-qubit gate, as well as laser cooling techniques. For example, the Mølmer-Sørensen entangling gate (Sørensen and Mølmer [2000]) is realised, in the traditional set-up, using detuned sideband coupling of the above form (5.10 - 5.11).

In summary, the Hamiltonians (5.9 - 5.11) collectively enable the realisation of all the techniques leading to universal quantum computation.

5.3 Introducing the magnetic gradient

Hamiltonians (5.10-5.11), which enable the coupling of electronic and motional states of the ion chain, are crucial for the realisation of quantum computing. It is seen that the strength of these interactions is governed by the Lamb-Dicke parameter, which in the derivation is assumed to be

small but non-zero. Physically, considering a semi-classical picture, η (5.4) is proportional to the ratio of the spatial extent of the ion in the harmonic trap to the wavelength of the radiation used for addressing. This is seen by computing the root-mean-square value of z for the Fock state with phonon number n (using (5.3)):

$$\Delta z = \sqrt{\langle n|z^2|n\rangle} = \zeta\sqrt{\frac{1}{2m\nu}} \cdot \sqrt{2n+1} \tag{5.12}$$

As the physical intuition would suggest, non-zero value for η signals the possibility of coupling the motional and the electronic states by an appropriate pulse. On the other hand, setting $\eta = 0$ in (5.8), it is seen that one would recover only the basic dipole Hamiltonian presented previously (2.13) (where the laser phase is added explicitly).

Considering the definition of η (5.4), it will be found that for realistic trap frequencies and microwave radiation wavelength, the parameter is vanishingly small (Mintert and Wunderlich [2001]). Moreover, individual addressing of the trapped particles in physical space would also become an extremely difficult task to perform with microwaves or radio waves. These are serious obstacles, which highlight the need for novel design.

In 2001, a proposal was made (Mintert and Wunderlich [2001]) for the addition of magnetic gradient along the trap axis to modify the interactions within the ion chain. Logical qubits would be encoded in a pair of magnetic-sensitive atomic levels, so that the energy spacing for the individual particles would vary along the trap axis following the gradient. As will be shown, this design overcomes the obstacle of η being essentially zero for RF/MW frequencies. Moreover, because each particle now has a different resonance frequency, individual addressing of the ions also becomes feasible even with long-wavelength radiation, which cannot be tightly focused. Experimentally, the constant magnetic field gradient can be realised using a pair of anti-Helmholtz coils, or more advanced techniques.

Figure 5.1 illustrates the basic physical intuition for coupling to the motional mode in such an arrangement. Each ion of the chain is now confined in a potential that is a sum of the harmonic term, arising from the Coulomb force and electrode confinement, and a linear term, which is the Zeeman effect due to the spatially varying magnetic field (the two effects sum to

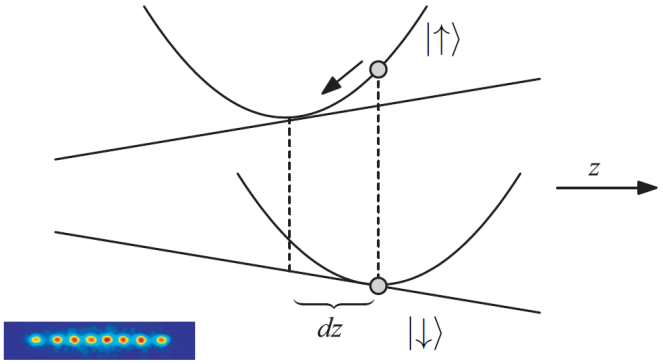

Figure 5.1: Potential-energy plots for a Zeeman-sensitive trapped-ion qubit in the presence of a magnetic gradient (Blatt and Wineland [2008]; Johanning et al. [2009b]).

give a quadratic potential of two different locations). Crucially, the sign of the linear term depends on the qubit state. The equilibrium position of the qubit depends on the sum of the two potential-energy contributions and is shifted by an amount dz in going from the ground to the excited state. This way, an internal excitation can cause the particle to be on the slope of its confining potential and induce spatial oscillations, thereby creating effective coupling between the electronic and the motional states (Johanning et al. [2009b]). This qualitatively new effect for attaining sideband coupling will be examined in mathematical detail in the following section.

5.4 The Hamiltonian for ion-field coupling with added gradient

This section reviews in detail the mathematics of ion-field coupling in the presence of a magnetic-field gradient. The derivation follows the steps of Mintert and Wunderlich [2001] (hereafter: Mintert&Wunderlich) and attempts to clarify the detailed calculations and the approximations made. Erratum in the derivation has been published (Mintert and Wunderlich [2003]). A more generalised derivation for the same physical system has also been published (Wunderlich [2002]).

We begin by quoting the phonon operator commutation relations:

$$[b, b^\dagger] = 1 \quad , \quad [b^\dagger, b] = -1. \tag{5.13}$$

Also, the Baker-Campbell-Hausdorff (BCH) formula will be used extensively:

$$e^X Y e^{-X} = Y + [X, Y] + \frac{1}{2!}[X, [X, Y]] + .. \tag{5.14}$$

5.4.1 First expressions

A linearly varying magnetic field is set up along the trap axis. The atomic energy levels are affected by the magnetic field in a linear fashion via the Zeeman effect. Hence, the energy gap $\omega(z)$ between the atomic levels is a linear function of displacement z, and the constant gradient for this function can be found. The free Hamiltonian for an atom in the particular vibrational mode reads:

$$H = \frac{1}{2}\,\omega(z)\sigma_z + \nu b^\dagger b \tag{5.15}$$

Expanding $\omega(z)$ about the ion's equilibrium position to first order:

$$H = \frac{1}{2}\omega_0\sigma_z + \frac{1}{2}\Big(\partial_z\omega(z)\cdot z\Big)\sigma_z + \nu b^\dagger b \tag{5.16}$$

Using (5.3) to rewrite the second term:

$$\frac{1}{2}\Big(\partial_z\omega(z)\cdot\zeta\sqrt{\frac{1}{2m\nu}}\cdot(b^\dagger + b)\Big)\sigma_z \tag{5.17}$$

and introducing the definition

$$\varepsilon_c = \partial_z\omega(z)\cdot\zeta\sqrt{\frac{1}{2m\nu}}\cdot\frac{1}{\nu} \tag{5.18}$$

one can write:

$$H = \frac{1}{2}\omega_0\sigma_z + \frac{1}{2}\nu\varepsilon_c(b^\dagger + b)\sigma_z + \nu b^\dagger b \tag{5.19}$$

This corresponds to Mintert&Wunderlich equation (1).

As previously, dipole Hamiltonian is introduced to model the interaction with the light field. The following needs to be added to (5.19):

$$H_M = \frac{\Omega}{2}(\sigma_+ + \sigma_-)(e^{i(kz-\omega_M t)} + h.c.) \tag{5.20}$$

One uses the relation found previously:

$$kz = \eta(b^\dagger + b) \tag{5.21}$$

to rewrite the dipole Hamiltonian. This gives:

$$H_M = \frac{\Omega}{2}(\sigma_+ + \sigma_-)(e^{i(\eta(b^\dagger+b)-\omega_M t)} + h.c.) \tag{5.22}$$

in correspondence with Mintert&Wunderlich equation (2). The full Hamiltonian is given by summing $H + H_M$.

5.4.2 Schrieffer–Wolff transformation

One modifies H and H_M by applying the transformation (Bravyi et al. [2011]) $\tilde{M} = e^S M e^{-S}$, where:

$$S = \frac{1}{2}\varepsilon_c(b^\dagger - b)\sigma_z \tag{5.23}$$

We first modify H (eq. (5.19)) by considering the effect of the transformation on each term. Essential use is made of the BCH formula (5.14), which relates transformations of the above kind to infinite series of nested commutators. It proves useful to compile the following 'dictionary':

$$e^{\frac{1}{2}\varepsilon_c(b^\dagger-b)\sigma_z}\left(\sigma_z\right)e^{-\frac{1}{2}\varepsilon_c(b^\dagger-b)\sigma_z} = \sigma_z \tag{5.24}$$

$$e^{\frac{1}{2}\varepsilon_c(b^\dagger-b)\sigma_z}\left(b^\dagger\right)e^{-\frac{1}{2}\varepsilon_c(b^\dagger-b)\sigma_z} = b^\dagger - \frac{1}{2}\varepsilon_c\sigma_z \tag{5.25}$$

$$e^{\frac{1}{2}\varepsilon_c(b^\dagger-b)\sigma_z}\left(b\right)e^{-\frac{1}{2}\varepsilon_c(b^\dagger-b)\sigma_z} = b - \frac{1}{2}\varepsilon_c\sigma_z \tag{5.26}$$

A term such as $b^\dagger b$ can be transformed by considering $e^S b^\dagger e^{-S} \cdot e^S b e^{-S}$. One

transforms equation (5.19) to obtain:

$$\tilde{H} = \frac{1}{2}\omega_0\sigma_z + \tag{5.27}$$

$$\frac{1}{2}\nu\varepsilon_c(b^\dagger + b)\sigma_z - \frac{1}{2}\nu\varepsilon_c^2 + \tag{5.28}$$

$$\nu(b^\dagger b) - \frac{1}{2}\nu\varepsilon_c(b^\dagger + b)\sigma_z + \frac{1}{4}\nu\varepsilon_c^2 = \tag{5.29}$$

$$= \frac{1}{2}\omega_0\sigma_z + \nu(b^\dagger b) \tag{5.30}$$

Here, σ_z^2 terms have been omitted since they represent just an identity operation. Also, in the last step a constant term $-\frac{1}{4}\nu\varepsilon_c^2$ has been dropped, since it represents merely a constant addition to all the energy eigenvalues.

Next, we transform H_M (eq. (5.22)) with the help of the following:

$$[\sigma_z, \sigma_+] = 2\sigma_+ \tag{5.31}$$

$$e^{\frac{1}{2}\varepsilon_c(b^\dagger - b)\sigma_z}\Big(\sigma_+\Big)e^{-\frac{1}{2}\varepsilon_c(b^\dagger - b)\sigma_z} = \sigma_+ + \varepsilon_c(b^\dagger - b)\sigma_+ + \frac{1}{2}\varepsilon_c^2(b^\dagger - b)^2\sigma_+ ...$$

$$= \sigma_+ e^{\varepsilon_c(b^\dagger - b)} \tag{5.32}$$

$$e^{\frac{1}{2}\varepsilon_c(b^\dagger - b)\sigma_z}\Big(\sigma_-\Big)e^{-\frac{1}{2}\varepsilon_c(b^\dagger - b)\sigma_z} = \sigma_- e^{-\varepsilon_c(b^\dagger - b)} \tag{5.33}$$

$$e^{\frac{1}{2}\varepsilon_c(b^\dagger - b)\sigma_z}\Big(k(b^\dagger + b)\Big)e^{-\frac{1}{2}\varepsilon_c(b^\dagger - b)\sigma_z} = k(b^\dagger + b - \varepsilon_c\sigma_z) \tag{5.34}$$

The first bracket in (5.22) is tackled separately, recalling that $\tilde{MN} = e^S M e^{-S} \cdot e^S N e^{-S}$. This also helps to transform the second bracket - one does this by expanding $e^{i\eta(b+b^\dagger)}$ in power series and applying (5.34) repeatedly.

With these considerations:

$$\tilde{H}_M = \frac{\Omega}{2}\Big(\sigma_+ e^{\varepsilon_c(b^\dagger - b)} + \sigma_- e^{-\varepsilon_c(b^\dagger - b)}\Big)\cdot$$

$$\Big[e^{-i\omega_M t}\Big(1 + i\eta(b^\dagger + b - \varepsilon_c\sigma_z) + \frac{(i\eta)^2}{2!}(b^\dagger + b - \varepsilon_c\sigma_z)^2 + ...\Big) + h.c.\Big] =$$

$$= \frac{\Omega}{2}\Big(\sigma_+ e^{\varepsilon_c(b^\dagger - b)} + \sigma_- e^{-\varepsilon_c(b^\dagger - b)}\Big)\cdot\Big(e^{i\eta(b^\dagger + b - \varepsilon_c\sigma_z) - i\omega_M t} + h.c.\Big) \tag{5.35}$$

Results (5.30) and (5.35) match those obtained in Mintert&Wunderlich (e.g. equation (3)).

5.4.3 Interaction picture and approximations

Taking the full Hamiltonian to be $\tilde{H} + \tilde{H}_M$, one moves to the interaction picture, treating $\tilde{H}_M$ as the coupling term. The following needs to be calculated (using (5.30) and (5.35)):

$$\tilde{H}_{int} = e^{i\tilde{H}t}\tilde{H}_M e^{-i\tilde{H}t} \tag{5.36}$$

It is once again handy to compile a 'dictionary':

$$[\sigma_z, \sigma_+] = 2\sigma_+ \tag{5.37}$$

$$e^{i\tilde{H}t}\Big(\sigma_+\Big)e^{-i\tilde{H}t} = e^{it(\frac{1}{2}\omega_0\sigma_z+\nu b^\dagger b)}\Big(\sigma_+\Big)e^{-it(\frac{1}{2}\omega_0\sigma_z+\nu b^\dagger b)} = \sigma_+ + (it\omega_o)\sigma_+ ...$$

$$= \sigma_+ e^{it\omega_0} \tag{5.38}$$

$$e^{it(\frac{1}{2}\omega_0\sigma_z+\nu b^\dagger b)}\Big(\sigma_z\Big)e^{-it(\frac{1}{2}\omega_0\sigma_z+\nu b^\dagger b)} = \sigma_z \tag{5.39}$$

$$[b^\dagger b, b^\dagger] = b^\dagger \tag{5.40}$$

$$e^{it(\frac{1}{2}\omega_0\sigma_z+\nu b^\dagger b)}\Big(b^\dagger\Big)e^{-it(\frac{1}{2}\omega_0\sigma_z+\nu b^\dagger b)} = b^\dagger + (it\nu)b^\dagger + .. = b^\dagger e^{it\nu} \tag{5.41}$$

$$e^{it(\frac{1}{2}\omega_0\sigma_z+\nu b^\dagger b)}\Big(b\Big)e^{-it(\frac{1}{2}\omega_0\sigma_z+\nu b^\dagger b)} = be^{-it\nu} \tag{5.42}$$

From (5.35) - and opening the brackets - it is clear that four terms will need to be evaluated. It is useful to work out the following transformations:

$$e^{it(\frac{1}{2}\omega_0\sigma_z+\nu b^\dagger b)}\Big(e^{k(b^\dagger \pm b)}\Big)e^{-it(\frac{1}{2}\omega_0\sigma_z+\nu b^\dagger b)} = e^{k(b^\dagger e^{it\nu} \pm b e^{-it\nu})} \tag{5.43}$$

$$e^{it(\frac{1}{2}\omega_0\sigma_z+\nu b^\dagger b)}\Big(e^{k\sigma_z}\Big)e^{-it(\frac{1}{2}\omega_0\sigma_z+\nu b^\dagger b)} = e^{k\sigma_z} \tag{5.44}$$

This enables one to calculate the first term of (5.35 - open brackets):

$$\tilde{H}_{int:1} = e^{i\tilde{H}t}\left(\frac{1}{2}\Omega\sigma_+ e^{\varepsilon_c(b^\dagger - b)} \cdot e^{i\eta(b^\dagger + b - \varepsilon_c\sigma_z) - i\omega_M t}\right)e^{-i\tilde{H}t} = \tag{5.45}$$

$$e^{i\tilde{H}t}\left(\frac{1}{2}\Omega \cdot \sigma_+ \cdot e^{-i\omega_M t} \cdot e^{-i\eta\varepsilon_c\sigma_z} \cdot e^{\varepsilon_c(b^\dagger - b)} e^{i\eta(b^\dagger + b)}\right)e^{-i\tilde{H}t} = \tag{5.46}$$

$$\frac{1}{2}\Omega \cdot \sigma_+ e^{it\omega_0} \cdot e^{-i\omega_M t} \cdot e^{-i\eta\varepsilon_c\sigma_z} \cdot e^{\varepsilon_c(b^\dagger e^{it\nu} - be^{-it\nu})} e^{i\eta(b^\dagger e^{it\nu} + be^{-it\nu})} = \tag{5.47}$$

$$= \frac{1}{2}\Omega \cdot \sigma_+ e^{i(\omega_0 - \omega_M)t} e^{-i\eta\varepsilon_c\sigma_z} \cdot e^{\varepsilon_c(\tilde{b}^\dagger - \tilde{b})} e^{i\eta(\tilde{b}^\dagger + \tilde{b})} \tag{5.48}$$

In the last step we have used $\tilde{b}^\dagger$ and $\tilde{b}$ defined previously (4.1).

A number of approximations are now applied:

- ε_c and η are taken to be small in the present context. One can thus use an approximation for non-commuting operators a, $a^\dagger$:

  $$e^{c(a^\dagger - a)} e^{d(a^\dagger + a)} \approx e^{(d-c)a + (c+d)a^\dagger} \tag{5.49}$$

  to first order in c and d.

  Accordingly, we combine the exponentials containing $\tilde{b}^\dagger$ and $\tilde{b}$ in (5.48) to yield: $e^{i(\eta + i\varepsilon_c)\tilde{b} + i(\eta - i\varepsilon_c)\tilde{b}^\dagger}$.

- The $e^{-i\eta\varepsilon_c\sigma_z}$ term is approximated to 1, in accordance with ε_c and η both being small.

- Of the four terms making up $\tilde{H}_{int}$ we only wish to keep the two that oscillate with $e^{\pm i(\omega_0 - \omega_M)t}$, eliminating the other two under RWA. The term $\tilde{H}_{int:1}$ is kept and one other term.

  Summarising the above points, one obtains the expression:

  $$\tilde{H}_{int} = \frac{\Omega}{2}\left(\sigma_+ e^{i\Delta t} \cdot e^{i(\eta + i\varepsilon_c)\tilde{b} + i(\eta - i\varepsilon_c)\tilde{b}^\dagger} + h.c.\right). \tag{5.50}$$

  This can be compared with Mintert&Wunderlich equation (4).

- The terms $\eta \pm i\varepsilon_c$ are rewritten as $\eta' e^{\pm i\phi}$ (η' and ϕ defined the obvious way). This leads, in (5.50), to the expression in the exponent:

$$i\eta' e^{i\phi} b e^{-it\nu} + i\eta' e^{-i\phi} b^\dagger e^{it\nu} \tag{5.51}$$

  The phase factors containing ϕ can be canceled by modifying the definition of the interaction picture. Instead of (5.36), one is free to consider an equivalent (up to a phase) transformation:

$$\tilde{H}_{int} = e^{i\tilde{H}(t+\phi/\nu)} \tilde{H}_M e^{-i\tilde{H}(t+\phi/\nu)}. \tag{5.52}$$

  In other words, we shift the origin of the time axis by a constant amount.

  Considering (5.41) and (5.42), it is clear that this will exactly cancel the $e^{\pm i\phi}$ factors in (5.51). However, from (5.38) it is also clear that the exponential multiplying σ_+ needs to be modified as well.

Summarising these considerations, the following is obtained as the end result:

$$\tilde{H}_{int} = \frac{\Omega}{2}\left(\sigma_+ e^{i\Delta t} e^{i\gamma} \cdot e^{i\eta'(\tilde{b}+\tilde{b}^\dagger)} + h.c.\right) \tag{5.53}$$

Where we have used:

$$\begin{aligned} \gamma &= \phi \cdot \frac{\omega_0}{\nu} = \tan^{-1}\left(\frac{\varepsilon_c}{\eta}\right) \cdot \frac{\omega_0}{\nu} \\ \eta' &= \sqrt{\varepsilon_c^2 + \eta^2}. \end{aligned} \tag{5.54}$$

And η and ε_c have been introduced in (5.4) and (5.18).

5.5 Discussion, experimental confirmation

One can now compare the conventional ion-field Hamiltonian (5.7) with the one just derived (5.53). It is found that a Hamiltonian of essentially the

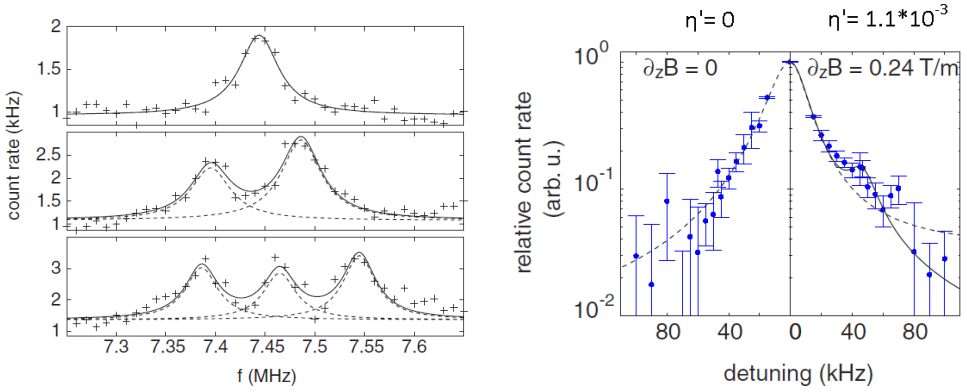

Figure 5.2: Addressing trapped Zeeman-sensitive ions with radio waves (Johanning et al. [2009a]). Left: evidence for individual addressing in frequency space. Luminiscence measurements for one, two and three particles in the trap with the addressing field frequency varied along the x-axis. Right: evidence for a motional sideband. Luminiscence measurements for a single trapped particle with and without the magnetic gradient being present.

same form emerges out of the calculation. The two notable modifications are, first, the $e^{i\gamma}$ factor, which can be compensated by the laser phase (we have omitted the laser phase from the derivation of the previous section for purposes of clarity). Secondly, it is the η' factor, introduced in (5.54), which takes the place of η.

The emergence of η' confirms the qualitative intuition given previously: that a further physical process has been introduced in the mechanism of coupling the electronic and the motional states. This is evident from the parameter η' being composed of two contributions (5.54). The welcome consequence is that now sideband coupling has become feasible even in circumstances where the conventional Lamb-Dicke parameter η is essentially zero. This opens the possibility for the usage of long-wavelength radiation.

The second issue that needed resolving – individual addressing – has also now been given a remedy. Because magnetic-sensitive levels are being used along with the magnetic gradient, the resonance frequencies will vary from particle to particle. This opens the possibility for individual addressing in frequency space, not physical space.

Experimental confirmation for both these ideas is reported in Johanning

et al. [2009a], where individual addressing of ions in frequency space and coupling of motional and internal states have been conclusively demonstrated. The experiments have been carried out on trapped $^{172}Yb^{+}$ ions using a pair of Zeeman-sensitive levels. Radio frequency driving field in the range of 7.5 MHz has been employed. The experiment has used a magnetic field of gradient estimated to be in the range of $0.2 - 0.5$ T/m.

Figure 5.2 left shows the evidence for successful individual addressing of the trapped particles. The three panels correspond to cases of one, two and three particles stored in the trap. As the addressing frequency is altered (horizontal axis), one ion after the other is seen to come into resonance with well-resolved peaks.

Figure 5.2 right shows evidence for the presence of a motional sideband. The results of scanning the resonance of a single particle are given, with zero magnetic gradient on the left hand side, and a non-zero gradient on the right hand side. In the latter case, experimental parameters give an appreciable value for the effective Lamb-Dicke parameter η' as indicated at the top. The visual evidence for a motional sideband has been supported by statistical analysis. The detuning at which the sideband occurs matches closely with the axial trap frequency, which can be established from the experimental parameters. This provides strong evidence for the attainment of coupling between internal and motional states.

5.6 Introducing the dressed states

The magnetic-gradient-induced coupling scheme is a major advancement towards long-wavelength quantum computing with trapped ions. As discussed, the beneficial effects of magnetic gradient serve both to make coupling of motional and spin states possible even for long wavelengths of the light field, and to resolve the issue of individual addressing.

However, there is a third issue to be considered, which stems from the effects of magnetic noise. The magnetic-gradient scheme is possible only with the usage of magnetic-sensitive states for the construction of the logical qubit, but there will unavoidably be the effects of magnetic noise in any laboratory setting, which would pose a serious challenge. Encoding the logical qubit in magnetically sensitive energy levels risks exposing the

scheme to serious vulnerability from such effects of random fluctuations.

A number of potential remedies have been proposed for dealing with such noise issues. Pulsed decoupling (Viola and Lloyd [1998]; Wokaun et al. [1987]) provides one possible strategy. Alternatively, the usage of dressed states for encoding the logical qubit (Jonathan and Plenio [2001]; Jonathan et al. [2000]; Retzker and Plenio [2007]) offers a possible shielding technique. The dressed-state approach has previously found applications in resonator and nitrogen vacancy systems (Bermudez et al. [2011]; Cai et al. [2012a, 2013, 2012b]; Rabl et al. [2009]) in addition to novel quantum gate designs for trapped ions using laser and laser-microwave addressing (Bermudez et al. [2012]; Lemmer et al. [2013]). Notably, the dressed-state approach in the context of long-wavelength quantum computing with static magnetic gradients was explored by Timoney et al. [2011], demonstrating experimentally its feasibility. Improvements in qubit coherence times by more than two orders of magnitude were reported.

This exciting development holds the promise of robust, long-wavelength quantum computation and will be the central theme for the remainder of this thesis. We will demonstrate in detail how the shielding is accomplished using the dressed states and we will propose quantum operations that jointly enable the execution of universal quantum computation within the dressed-state design.

Basic single-qubit operations for this set-up have been realised by Timoney et al. [2011] and also by Webster et al. [2013] in a slightly modified arrangement. We will develop in detail the set-up employed by Timoney et al. [2011] and propose a set of novel quantum operations. Firstly, we show how to realise arbitrary single-qubit rotations, proposing several alternative gate schemes. Secondly, following the well-known scheme of Sørensen and Mølmer [1999, 2000], we develop a two-qubit entangling gate. We simulate the gates numerically to demonstrate their experimental viability and present analysis of the key noise sources. Finally, we comment on the possibilities for extending our scheme to the experimental set-up employed by Webster et al. [2013].

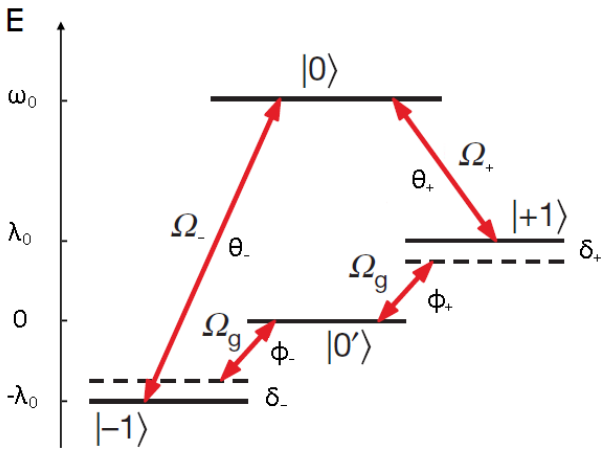

Figure 5.3: Four-level system for the realisation of the dressed state qubit, together with couplings in the microwave and radio wave domain ($\Omega_{+/-}$ and Ω_g respectively). Rabi frequencies are denoted by Ω_i, detunings by δ_i and laser phases by θ_i, ϕ_i. Another possible coupling not shown is between $|0\rangle$ and $|0'\rangle$, which is described using Ω_z, θ_z and δ_z. States $|-1\rangle$ and $|1\rangle$ are the magnetic-sensitive levels, and the presence of a positive static magnetic field is assumed.

5.6.1 Physical set-up

Our gate scheme retains all the key elements of the original proposal by Timoney et al. [2011] (also described in Webster et al. [2013]). The particular candidate for experimental implementation is trapped $^{171}Yb^+$ ions, however, the gate derivations will be presented for a generic magnetic-sensitive four-level system, depicted in Figure 5.3. States $|-1\rangle$ and $|1\rangle$ are the magnetic-sensitive levels, and the presence of static magnetic field generates their splitting in energy. The $|-1\rangle \leftrightarrow |1\rangle$ transition is considered forbidden in analogy with the $^{171}Yb^+$ case (see section 2.4).

One creates dressed states by means of a partial STIRAP sequence (see section 2.5) from either $|-1\rangle$ or $|1\rangle$ as the original state and $|0\rangle$ as the intermediate state. Using the microwave fields $\Omega_{+/-}$ for the realisation of STIRAP, the sequence is halted in the middle, leaving the fields on at constant strength. Choosing appropriate field phases enables one to reach

either of the dressed states:

$$|D\rangle = \frac{1}{\sqrt{2}}(|-1\rangle - |1\rangle)$$
$$|B\rangle = \frac{1}{\sqrt{2}}(|-1\rangle + |1\rangle). \tag{5.55}$$

Experimental creation of such states has been achieved using $^{171}Yb^{+}$ ions with lifetimes in excess of $500ms$ (Timoney et al. [2011]; Webster et al. [2013]).

Quantum operations are to be carried out using either $\{|D\rangle, |0'\rangle\}$ or $\{|B\rangle, |0'\rangle\}$ as the logical qubit. The four-state system is viewed in either case by considering the remaining pair of orthogonal states: $\{|B\rangle, |0\rangle\}$ and $\{|D\rangle, |0\rangle\}$, respectively. We also define 'up' and 'down' as alternative basis states, which will be important in the discussion:

For the D-qubit:	For the B-qubit:
$\|u\rangle = \frac{1}{\sqrt{2}}(\|B\rangle + \|0\rangle)$	$\|u\rangle = \frac{1}{\sqrt{2}}(\|D\rangle + \|0\rangle)$
$\|d\rangle = \frac{1}{\sqrt{2}}(\|B\rangle - \|0\rangle)$	$\|d\rangle = \frac{1}{\sqrt{2}}(\|D\rangle - \|0\rangle).$

(5.56)

During the halted STIRAP sequence, with the dressing fields constant at $\Omega_{+/-} = \Omega$, it will be found that $|u\rangle$ and $|d\rangle$ diagonalise the Hamiltonian. Figure 5.4 plots the energy level diagram for the D-qubit case, showing how an energy gap is opened between the qubit space and the states $|u\rangle$ and $|d\rangle$. As will be demonstrated in the following chapters, this energy gap provides the crucial ingredient for suppressing the effects of magnetic noise. This way, a robust and shielded qubit can be realised. Interactions within the qubit space can be driven by introducing additional RF fields (Rabi frequency Ω_g). After the quantum operations have been performed, read-out would be performed by completing the STIRAP sequence and carrying out a fluorescence measurement.

It will be illustrated how single and multi-qubit gates can be realised in such a set-up, using, for the multi-qubit case, the magnetic-gradient-induced coupling discussed previously. In contrast to recent experimental work, where second-order energy level shifts in response to magnetic field

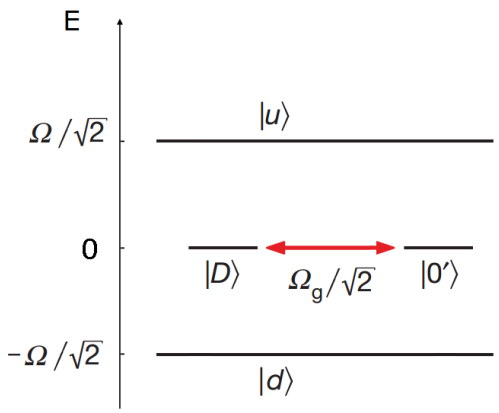

Figure 5.4: Viewing the physical system (Figure 5.3) in the dressed-state basis, taking the example of the D-qubit. Microwave dressing fields are held constant at $\Omega_{+/-} = \Omega$, and the dressed states are defined using (5.55) and (5.56). Analogous arrangement is found for the B-qubit.

are intrinsically used (Webster et al. [2013]), we show how the simple linear Zeeman shift is sufficient to construct a universal gate set. Further, we ease the experimental requirements by setting equal the phases and detunings of the RF fields: $\phi_- = \phi_+$, $\delta_- = \delta_+$ (using distinct values for the hyperfine ground state of $^{171}Yb^+$ would be possible, in principle, using polarisation). In other words, the RF couplings in Figure 5.3 would be created by a single field interacting with both $|-1\rangle \leftrightarrow |0'\rangle$ and $|0'\rangle \leftrightarrow |1\rangle$ pairs of levels simultaneously. In the case of the two-qubit gate (chapter 7), interactions will be created by two radio frequency fields per qubit, each interacting with both pairs of levels, thus generating four couplings per trapped particle.

Having demonstrated the scheme in detail, we discuss the case of prominent non-linear energy level response (chapter 8), considering modifications of our designs in light of the greater experimental facility.

Chapter 6

Single-qubit operations

The previous chapter has demonstrated how the addition of static magnetic gradient renders long-wavelength quantum computation theoretically possible. Also, the idea of using dressed states has been introduced. There remains the challenge of demonstrating that universal quantum computation would indeed be possible in the dressed-state basis. For this purpose, one needs to design a universal set of single-qubit operations, as well as a multi-qubit entangling gate (Nielsen and Chuang [2010]). This chapter demonstrates the feasibility of attaining universal single-qubit rotations within the dressed-state set-up. We propose a set of quantum techniques and analyse in detail their sensitivity to experimental noise both theoretically and with the help of numerical simulation, showing how the desired shielding effect is indeed accomplished.

We propose and describe two distinct gates (sections 6.2, 6.4) as well as an adiabatic transfer technique (section 6.3). Further, we present in less detail two additional single-qubit gate designs (section 6.5), which possess slightly less favourable properties but will be useful in later discussion.

Considering the eventual experimental implementation, within the set-up of an ion chain, addressing of individual qubits would be accomplished by separation in frequency space with the help of static magnetic gradient. This relies on gates coupling only such pairs of levels, where at least one state is magnetically sensitive, so that resonant frequencies vary along the trap axis. The main gate designs proposed in this chapter do retain such a property.

As the two key limiting factors to gate fidelity, we consider explicitly the noise in the ambient magnetic field and noise due to the instability of the microwave dressing frequencies $\Omega_{+/-}$. It will be shown how these effects can be overcome to reach gate fidelities in excess of 99% in numerical simulation. In order to maintain analytical tractability and illustrate precisely the role of the two sources of experimental noise, the single-qubit gates will be presented and analysed in the slightly simplified set-up with zero magnetic gradient present in the trap. Section 6.7 provides justification for regarding the gradient a negligible effect for the single-qubit gates.

This chapter is original research work, except where referenced otherwise. Both original theoretical calculations and simulations have been performed.

6.1 Hamiltonian and noise sources

We write down the single-particle Hamiltonian of the most general useful form. Figure 5.3 defines the phases, detunings and Rabi frequencies used. An extra possibility not drawn for clarity of presentation is the coupling between $|0\rangle$ and $|0'\rangle$, which is defined using Ω_z, θ_z, and δ_z. Within the dipole approximation (see section 2.1), one obtains the following expression:

$$H = \omega_0|0\rangle\langle 0| + \lambda_0|1\rangle\langle 1| - \lambda_0|-1\rangle\langle -1| + \tag{6.1}$$

$$\Omega_- \cos\Big((\omega_0 + \lambda_0)t + \theta_-\Big)|-1\rangle\langle 0| +$$

$$\Omega_+ \cos\Big((\omega_0 - \lambda_0)t + \theta_+\Big)|1\rangle\langle 0| + h.c. + \tag{6.2}$$

$$\Omega_g \cos\Big((\lambda_0 - \delta_-)t + \phi_-\Big)|-1\rangle\langle 0'| +$$

$$\Omega_g \cos\Big((\lambda_0 - \delta_+)t + \phi_+\Big)|1\rangle\langle 0'| + h.c. + \tag{6.3}$$

$$\Omega_z \cos\Big((\omega_0 - \delta_z)t + \theta_z\Big)|0'\rangle\langle 0| + h.c. \tag{6.4}$$

Moving to the interaction picture with respect to the time-independent part (6.1) and performing the RWA:

$$H = \frac{1}{2}\Bigg(e^{-i\theta_-}\Omega_-|0\rangle\langle -1| + e^{-i\theta_+}\Omega_+|0\rangle\langle 1| + \\ e^{i\phi_- - i\delta_- t}\Omega_g|-1\rangle\langle 0'| + e^{i\phi_+ - i\delta_+ t}\Omega_g|0'\rangle\langle 1| + \\ e^{-i\theta_z + i\delta_z t}\Omega_z|0\rangle\langle 0'|\Bigg) + h.c. \tag{6.5}$$

Magnetic fluctuations are introduced by considering the additional term in the Hamiltonian, affecting the two magnetic-sensitive states:

$$\mu(t)\Big(|1\rangle\langle 1| - |-1\rangle\langle -1|\Big) \tag{6.6}$$

with $\mu(t)$ being a stochastic process of amplitude proportional to fluctuations in the ambient magnetic field.

Regarding the noise in $\Omega_{+/-}$, we approximate and define:

$$\Omega_- + \Omega_+ \approx 2\Omega \\ \Omega_- - \Omega_+ = \delta_\Omega \tag{6.7}$$

where Ω is taken as constant and δ_Ω is a second stochastic process. Since the radio frequency couplings will be generated, in the one-qubit case, by a single field, no analogous term is introduced for Ω_g.

The magnitude of the magnetic noise term μ can be quantified by its standard deviation SD_μ. Section 6.6 provides an estimate for this parameter, based on experimental measurements, of $2\pi \cdot 88$ Hz. In numerical simulation (section 6.6), SD_μ will be set constant to this value.

In contrast, the magnitude of δ_Ω is modeled as being proportional to Ω. One can assume normally distributed noise in the strength of the microwave fields $\Omega_{+/-}$ with standard deviation $f\Omega$. Experimentally, Ω_- and Ω_+ can be generated from the same microwave source that is multiplied by a radio frequency driving field. In that case, the noise in the microwave Rabi frequencies would be strongly correlated. However, under the extreme assumption of complete independence between Ω_- and Ω_+, the standard

deviation of δ_Ω would equal $\sqrt{2}f\Omega$:

$$\begin{aligned} SD_\Omega &= f\Omega \\ SD_{\delta_\Omega} &= \sqrt{2}f\Omega. \end{aligned} \tag{6.8}$$

In the experimental context, correlation between Ω_- and Ω_+ would almost certainly reduce the value of SD_{δ_Ω} significantly. However, (6.8) will be used in calculations and numerical simulation because of computational simplicity and for reasons of conservative estimation.

6.2 Basic σ_x/σ_y gates

Building on the work of Timoney et al. [2011], it is shown how the σ_y gate for the D-qubit and the σ_x gate for the B-qubit can be realised by appropriate choice of field phases. Removing the $|0\rangle \leftrightarrow |0'\rangle$ coupling in (6.5) and choosing:

$$\begin{aligned} &\Omega_{+/-} = \Omega \\ &\theta_+ = 0 \ , \ \theta_- = 0 \\ &\phi_+ = \ \phi_- = \pi/2 \\ &\delta_+ = \ \delta_- = 0 \end{aligned} \tag{6.9}$$

one finds

$$\begin{aligned} H = &\frac{\Omega}{\sqrt{2}}\Big(|u\rangle\langle u| - |d\rangle\langle d|\Big) + \\ &\frac{\Omega_g}{\sqrt{2}}\Big(i|D\rangle\langle 0'| - i|0'\rangle\langle D|\Big). \end{aligned} \tag{6.10}$$

And setting:

$$\begin{aligned} &\Omega_{+/-} = \Omega \\ &\theta_+ = \pi \ , \ \theta_- = 0 \\ &\phi_+ = \ \phi_- = 0 \\ &\delta_+ = \ \delta_- = 0 \end{aligned} \tag{6.11}$$

one obtains

$$H = \frac{\Omega}{\sqrt{2}}\left(|u\rangle\langle u| - |d\rangle\langle d|\right) + \frac{\Omega_g}{\sqrt{2}}\left(|B\rangle\langle 0'| + |0'\rangle\langle B|\right) \tag{6.12}$$

using the appropriate definitions of $|u\rangle$ and $|d\rangle$ (5.56).

It is seen that the radio wave part (Rabi frequency Ω_g) in the above expressions yields the sought-after forms for the single-qubit quantum gates, while microwave dressing fields (frequency Ω) separate the energies of the remaining pair of basis states. The case of the D-qubit (6.10) has been plotted previously in Figure 5.4. The energy gap opened by the microwave fields plays a crucial role in shielding the qubit, particularly against the magnetic noise effects. Such a mechanism is common to all the gates presented in this chapter and chapter 7, which rely on the dressed states.

Further examination reveals that the requirement to set equal the radio wave phases ($\phi_- = \phi_+$) allows for no other σ_i gate to be created using this route for either the B or the D-qubits. The scheme could be generalised to consider superpositions of states $|B\rangle$ and $|D\rangle$, so that the logical qubit would now be represented by $\{|0'\rangle, \cos\beta|B\rangle + \sin\beta|D\rangle\}$. In such a case, a single σ_β gate in the xy plane of the Bloch sphere becomes feasible for each choice of β. However, the technique allows for no second independent rotation to be achieved for the same definition of the logical qubit. Hence, complementary techniques will be required to realise universal single-qubit rotation.

Considering the D-qubit case and adding the two noise sources (6.6, 6.7), expression (6.10) remains unaltered, but it needs to be complemented by the following term:

$$H_n = \left(-\frac{\mu}{\sqrt{2}} + \frac{\delta_\Omega}{4}\right)|D\rangle\langle u| + \left(-\frac{\mu}{\sqrt{2}} - \frac{\delta_\Omega}{4}\right)|D\rangle\langle d| \; + \; h.c. \tag{6.13}$$

Moving to the interaction picture with respect to the microwave and radio wave part (6.10), one finds that rotating phases of frequency $(\Omega \pm \Omega_g)/\sqrt{2}$

are introduced to all terms in H_n (6.13). Therefore, provided that the magnitudes of μ, δ_Ω are much smaller than the rotation frequency, the terms can be deemed negligible within the rotating wave approximation.

The magnitude of H_n (in the interaction picture) can be further estimated by the Dyson series expansion (see section 2.2), writing the time-propagation operator $U(t)$ in orders of H_n and looking for terms that grow linearly with t (secular terms). In the second order, one recovers corrections to the energies of $|u\rangle$ and $|d\rangle$, in addition to terms in the qubit space:

$$\begin{aligned} H_{n2} =& \frac{\mu\Omega\delta_\Omega}{2(\Omega^2-\Omega_g^2)}\Big(|D\rangle\langle D| + |0'\rangle\langle 0'|\Big) \\ &+ i\frac{(8\mu^2+\delta_\Omega^2)\Omega_g}{8\sqrt{2}(-\Omega^2+\Omega_g^2)}\Big(|D\rangle\langle 0'| - |0'\rangle\langle D|\Big). \end{aligned} \tag{6.14}$$

This amounts to an energy shift and a correction to the σ_y gate couplings. In the third order, one finds population leakage terms out of the qubit space of magnitude:

$$\frac{\Omega^2(\sqrt{8}\mu \pm \delta_\Omega)^3}{32(\Omega^2-\Omega_g^2)^2} \quad , \quad \frac{\Omega\Omega_g(\sqrt{8}\mu \pm \delta_\Omega)^3}{32(\Omega^2-\Omega_g^2)^2}. \tag{6.15}$$

Minimisation of these unwanted terms can be accomplished by suppression through large denominator. The conditions for this can be summarised as:

$$\sqrt{|\Omega^2-\Omega_g^2|} \;\gg\; \{\mu, \delta_\Omega\}. \tag{6.16}$$

This is well within the experimental capability, as numerical simulation will demonstrate.

6.3 Adiabatic transfer between $|B\rangle$ and $|D\rangle$

The basic σ_x and σ_y gates can be linked for computational purposes by means of population transfer between $|B\rangle$ and $|D\rangle$. This is achieved by adiabatic variation of the microwave phase in a set-up that leaves $|0'\rangle$ decoupled.

Removing the $|0\rangle \leftrightarrow |0'\rangle$ coupling and the RF fields in (6.5), one sets

$\Omega_{+/-} = \Omega$. This provides the timescale on which adiabacity would be maintained. One also sets to zero one of the microwave phases: $\theta_- = 0$. The transfer is based on slow variation of the other microwave phase $\theta_+(t)$, such that the system is kept in the zero-eigenvalue state:

$$|\Psi_0(t)\rangle = \frac{1}{\sqrt{2}} \left(|-1\rangle - e^{i\theta_+}|1\rangle\right). \tag{6.17}$$

Moving from $|D\rangle$ to $|B\rangle$ is achieved by varying θ_+ from 0 to π and moving from $|B\rangle$ to $|D\rangle$ is obtained by varying the opposite way. Given that $|0'\rangle$ remains decoupled throughout, the following evolutions are enabled:

$$\begin{aligned} a|D\rangle + b|0'\rangle &\longrightarrow ae^{-i\pi/2}|B\rangle + b|0'\rangle \\ a|B\rangle + b|0'\rangle &\longrightarrow ae^{i\pi/2}|D\rangle + b|0'\rangle. \end{aligned} \tag{6.18}$$

The Berry's phase has been added in the expressions above, which can be calculated using standard formulae (see section 2.3). In the numerical simulations (section 6.6), we vary the microwave phase continuously over a greater range, which yields an outcome state that is a straightforward linear extension of (6.18).

To analyse the effects of noise, one views the system in the adiabatic basis $\{|0'\rangle, |\Psi_0\rangle, |u_{ad}\rangle, |d_{ad}\rangle\}$, where the noiseless Hamiltonian is diagonalised. The states $\{|0'\rangle, |\Psi_0\rangle\}$, which represent the qubit space, lie at zero energy, while the latter two time-dependent orthogonal eigenstates are found to lie at energies $\pm\Omega/\sqrt{2}$. This way, an energy gap is realised.

Applying the appropriate basis change to magnetic noise (6.6), and introducing effects due to microwave instability (6.7), one finds the following noise contribution:

$$\begin{aligned} H_n = \; & e^{-i\theta_+}\left(-\frac{\mu}{\sqrt{2}} + \frac{\delta_\Omega}{4}\right)|\Psi_0\rangle\langle u_{ad}| + \\ & e^{-i\theta_+}\left(-\frac{\mu}{\sqrt{2}} - \frac{\delta_\Omega}{4}\right)|\Psi_0\rangle\langle d_{ad}| \; + \; h.c. \end{aligned} \tag{6.19}$$

Moving to the interaction picture with respect to the noiseless Hamiltonian $(\Omega/\sqrt{2}) \cdot (|u_{ad}\rangle\langle u_{ad}| - |d_{ad}\rangle\langle d_{ad}|)$ will introduce rotations to all terms in H_n, making them negligible within the rotating wave approximation for

sufficiently large Ω.

Expanding the time-propagation operator in orders of H_n (in the interaction picture) and looking for secular terms, one finds in the second order a term affecting the qubit space:

$$H_{n2} = \frac{\mu\delta_\Omega}{\Omega}|\Psi_0\rangle\langle\Psi_0|. \tag{6.20}$$

The third order is found to contain leakage terms out of the qubit space of functional forms: μ^3/Ω^2, $\mu^2\delta_\Omega/\Omega^2$, $\mu\delta_\Omega^2/\Omega^2$, δ_Ω^3/Ω^2. Minimising these unwanted couplings requires:

$$\begin{aligned} &\Omega \gg SD_\mu \\ &f \ll 1. \end{aligned} \tag{6.21}$$

In contrast to the basic σ_i gates, where the speed is governed by the radio frequency fields, the maximum speed of adiabatic transfer is governed by Ω and the requirement for the evolution to remain adiabatic.

6.4 Adiabatic σ_z gate

We construct a σ_z gate based on adiabatic evolution and the Berry's phase. The gate idea follows the proposal by Duan et al. [2001], although it is modified in important ways to suit the present set-up and improve speed and resilience.

The gate is illustrated for the case of the D-qubit, noting that analogous construction also exists for the B-qubit. One removes the $|0\rangle \leftrightarrow |0'\rangle$ coupling in (6.5) and introduces adiabatic variables $R_1(t)$ and $R_2(t)$ as follows:

$$\begin{aligned} \Omega_{+/-} &= \Omega \sin(R_2) \\ \theta_- &= \theta_+ = R_1 \\ \Omega_g &= \Omega \cos(R_2) \\ \phi_- &= \phi_+ = 0 \\ \delta_+ &= \delta_- = 0. \end{aligned} \tag{6.22}$$

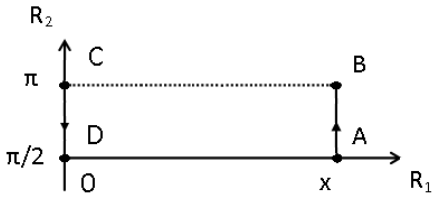

Figure 6.1: Proposed paths of the variables $R_{1,2}(t)$ (6.22) for the adiabatic σ_z gate. Detailed examination reveals that the segment $B \rightarrow C$ can be omitted.

Again, Ω fixes the adiabatic timescale for the gate.

Substituting into the noiseless Hamiltonian (6.5) one obtains:

$$H = \frac{\Omega e^{iR_1} \sin R_2}{\sqrt{2}} |B\rangle\langle 0| + \frac{\Omega \cos R_2}{\sqrt{2}} |B\rangle\langle 0'| \quad + \quad h.c. \tag{6.23}$$

It is seen that $|D\rangle$ remains decoupled. The σ_z gate will be created by inducing the Berry's phase in the $|0'\rangle$ component, effecting the following evolution:

$$a|D\rangle + b|0'\rangle \longrightarrow a|D\rangle + be^{i\Phi}|0'\rangle. \tag{6.24}$$

This will be enabled by the zero-energy eigenstate of (6.23):

$$|\Psi_0(t)\rangle = \; -e^{-iR_1} \cos R_2 \, |0\rangle + \sin R_2 \, |0'\rangle. \tag{6.25}$$

To begin and end at state $|0'\rangle$, any adiabatic evolution of $|\Psi_0(t)\rangle$ in the $\{R_1, R_2\}$ plane will need to begin and end on the line $R_2 = \pi/2$. The Berry's phase generated by any such trajectory can be calculated (see section 2.3):

$$\begin{aligned} \Phi = i \int_{\mathbf{R}_i}^{\mathbf{R}_f} \Big(\langle \Psi_0 | \partial_{R_1} | \Psi_0 \rangle dR_1 + \langle \Psi_0 | \partial_{R_2} | \Psi_0 \rangle dR_2 \Big) = \\ = \int_{\mathbf{R}_i}^{\mathbf{R}_f} (\cos R_2)^2 dR_1. \end{aligned} \tag{6.26}$$

For the purpose of gate speed, it is desirable to find a path that yields the maximum phase while traversing the least distance. It is seen from

(6.26) that moving along $R_2 = \pi/2$ will generate no extra phase. Figure 6.1 shows the path we propose, beginning at point A and ending at point D. Furthermore, the segment $B \to C$ is omitted, based on mathematical arguments.

One uses (6.26) to establish that no Berry's phase is generated along the segments $A \to B$ and $C \to D$. In contrast, the phase generated along $B \to C$ is found to be $\Phi = R_1(t) - x$. This cancels exactly the time evolution of $|\Psi_0\rangle$ (6.25), so that along $B \to C$ the state follows as:

$$|\Psi_0(t)\rangle_{BC} = \; e^{-ix}\,|0\rangle \tag{6.27}$$

displaying no time evolution. It is also seen that the Hamiltonian (6.23) effects no time evolution for $|\Psi_0\rangle$ along $B \to C$, irrespective of the range x.

These arguments allow one to cut out the segment $B \to C$ altogether, meaning that a trajectory of the same length can be traversed in the $\{R_1, R_2\}$ plane to induce arbitrary phase for the $|0'\rangle$ component. The total phase induced at the end of the path (see (6.24)) is found to be $\Phi = -x$.

For the purpose of noise analysis, the Hamiltonian is diagonalised using the adiabatic basis $\{|D\rangle, |\Psi_0\rangle, |u_{ad}\rangle, |d_{ad}\rangle\}$, where the latter two states are found to lie at energies $\pm\Omega/\sqrt{2}$. Applying the basis change to the noise contributions, the following term is found:

$$H_n = \; -\frac{\delta_\Omega \sin 2R_2}{4\sqrt{2}}|D\rangle\langle\Psi_0| \;+\; h.c. \;+ \tag{6.28}$$

$$\left(-\frac{\mu}{\sqrt{2}} + \frac{\delta_\Omega \sin R_2^2}{4}\right)|D\rangle\langle u_{ad}| + \left(\frac{\mu}{\sqrt{2}} + \frac{\delta_\Omega \sin R_2^2}{4}\right)|D\rangle\langle d_{ad}| \;+\; h.c. \tag{6.29}$$

Line (6.28) yields a first-order noise term within the qubit space that is not correctable by the dressing field.

After transforming H_n to the interaction picture with respect to the noiseless Hamiltonian $(\Omega/\sqrt{2}) \cdot (|u_{ad}\rangle\langle u_{ad}| - |d_{ad}\rangle\langle d_{ad}|)$, the following extra

contribution is found in the qubit space to second order:

$$H_{n2} = \frac{\mu\delta_\Omega \sin R_2^2}{\Omega}|D\rangle\langle D|. \tag{6.30}$$

Moreover, leakage terms of forms $\delta_\Omega\mu/\Omega, \delta_\Omega^2/\Omega$ are also recovered.

The dominant noise term is by far (6.28), which can be minimised by requiring good microwave stability ($f \ll 1$), and by lowering Ω (and hence SD_{δ_Ω} (6.8)). Considering the first and second order terms only would suggest that a choice of Ω as low as possible would minimise these lowest-order noise effects.

However, the third order analysis reveals terms that grow with reduced Ω. The following is found in the qubit space:

$$H_{n3} = \frac{\delta_\Omega(8\mu^2 + \delta_\Omega^2 \sin {R_2}^4) \sin 2R_2}{16\sqrt{2}\,\Omega^2}\,|D\rangle\langle\Psi_0| \;+\; h.c. \tag{6.31}$$

In addition, leakage terms of the following form are found: $\mu^3/\Omega^2, \mu^2\delta_\Omega/\Omega^2$, $\mu\delta_\Omega^2/\Omega^2, \delta_\Omega^3/\Omega^2$. The requirement to maintain negligible terms such as μ^3/Ω^2 sets a lower limit on Ω, suggesting the existence of an optimal microwave dressing frequency. This is further confirmed in the numerical analysis.

Noise minimisation would therefore be achieved for:

$$\begin{aligned} &\Omega = \Omega_{opt} \\ &f \ll 1. \end{aligned} \tag{6.32}$$

It will be shown in section 6.6.3 how a value for Ω_{opt} does indeed emerge numerically for different sets of simulation parameters. It is expected also within the experimental context that a value for Ω_{opt} can be found beyond which a reduction in fidelity occurs.

A further lower limit on Ω would be set by the desired gate speed and the adiabacity requirement.

6.5 Other σ_z gate designs

Other ways to realise the σ_z gate are briefly described, taking the example of the D-qubit. Firstly, it is possible to construct the adiabatic σ_z gate via two alternative routes. Section 6.4 has demonstrated how a phase in $|0'\rangle$ can be induced by employing couplings of the following form: $|0'\rangle \leftrightarrow |B\rangle \leftrightarrow |0\rangle$ (see (6.23)). Alternatively, one can induce the Berry's phase in $|0'\rangle$ by employing couplings of form $|0'\rangle \leftrightarrow |0\rangle \leftrightarrow |B\rangle$, in a set-up that uses $\Omega_{+/-}$ and Ω_z microwave fields. It is also possible to follow more closely the original proposal of Duan et al. [2001], using the following couplings: $|-1\rangle \leftrightarrow |0\rangle \leftrightarrow |1\rangle$. This arrangement would require microwave fields $\Omega_{+/-}$ only and work by inducing a phase in $|D\rangle$. The disadvantages found for these alternative schemes include lower gate speed, less favourable noise effects, and the need to couple two magnetically insensitive levels. The adiabatic gate presented in section 6.4 is found to possess the most favourable overall qualities. However, it is also acknowledged that other functional forms for introducing the adiabatic variables $\{R_1, R_2\}$ could be explored.

Secondly, it is also possible to use the effect of Stark shift (see section 2.1.3) to create the σ_z gate, a viable alternative to the adiabatic approach. We show two such designs in this section, the first of which relies on detuned $|0\rangle \leftrightarrow |0'\rangle$ coupling. It is shown how microwave dressing can be applied in such a case to shield the gate. The scheme would have the potential disadvantages of having to couple two magnetically insensitive levels, as well as having tighter experimental constraints on the parameters.

Likewise, we present a radio wave Stark shift σ_z gate that relies on $\{\phi_- \neq \phi_+, \delta_- \neq \delta_+\}$, which goes beyond the experimental limitations considered. The gate is added in light of extending the discussion to non-linear Zeeman regime (chapter 8), and is found to possess good overall properties.

6.5.1 σ_z gate via dressed $|0\rangle \leftrightarrow |0'\rangle$ Stark shift

Detuned $|0\rangle \leftrightarrow |0'\rangle$ coupling specified by Ω_z, δ_z and θ_z enables a phase to be induced in $|0'\rangle$ and a σ_z gate to be realised using the effect of Stark shift. It is shown how microwave dressing can be added to the process to protect it from noise effects.

Removing the radio frequency fields in (6.5) and setting for the D-qubit case:

$$\begin{aligned} \theta_z &= 0 \\ \Omega_{+/-} &= \Omega \\ \theta_- &= \theta_+ = 0 \end{aligned} \tag{6.33}$$

one moves to the dressed basis to obtain:

$$\begin{aligned} H = &\frac{\Omega}{\sqrt{2}} \Big(|u\rangle\langle u| - |d\rangle\langle d| \Big) + \\ &\frac{\Omega_z}{2\sqrt{2}} \Big(|u\rangle\langle 0'| e^{it\delta_z} - |d\rangle\langle 0'| e^{it\delta_z} \Big) \; + \; h.c. \end{aligned} \tag{6.34}$$

together with a noise contribution of form (6.13).

Moving to the interaction picture with respect to the Ω-term will cause the noise terms to rotate. In addition, the time-dependence in the term proportional to Ω_z in the expression above will be modified. It still creates a Stark-shift-like effect, modifying the energies of $|u\rangle$, $|d\rangle$ and $|0'\rangle$ in the second order of the Dyson series expansion. In particular, the addition to the qubit space takes the form:

$$H_{add} = \frac{\delta_z \Omega_z^2}{2\Omega^2 - 4\delta_z^2} \, |0'\rangle\langle 0'| \tag{6.35}$$

and enables a σ_z gate to be realised.

The two Stark-shift-like processes in the above derivation rely on the following experimental constraint:

$$|\Omega \pm \sqrt{2}\delta_z| \gg \Omega_z. \tag{6.36}$$

6.5.2 σ_z gate via radio wave Stark shift

A σ_z gate is presented that requires independent addressing by two separate RF fields. The D-qubit case is shown. Canceling the $|0\rangle \leftrightarrow |0'\rangle$ coupling

and setting in (6.5):

$$\begin{aligned}
&\Omega_{+/-} = \Omega \\
&\theta_- = \theta_+ = 0 \\
&\phi_+ = \pi \ , \ \phi_- = 0 \\
&\delta_+ = -\delta \ , \ \delta_- = \delta
\end{aligned} \tag{6.37}$$

one recovers

$$\begin{aligned}
H = &\frac{\Omega}{\sqrt{2}} \Big(|u\rangle\langle u| - |d\rangle\langle d| \Big) + \\
&\frac{\Omega_g}{\sqrt{2}} \Big(|0'\rangle\langle D| e^{i\delta t} + h.c. \Big).
\end{aligned} \tag{6.38}$$

The radio wave part yields the σ_z gate between $|D\rangle$ and $|0'\rangle$, using the standard Stark shift approximation (section 2.1.3):

$$H_{rw} \approx \frac{\Omega_g^2}{2\delta} \Big(|0'\rangle\langle 0'| - |D\rangle\langle D| \Big). \tag{6.39}$$

The condition of validity for the last step is:

$$\Omega_g \ll \delta. \tag{6.40}$$

6.6 Numerical simulation

Experimental noise in the magnetic field and in the microwave and radio wave Rabi frequencies is modeled as the Ornstein-Uhlenbeck process, using formulae found in Gillespie [1996a]. Two parameters need to be specified for each process: the relaxation time τ and the diffusion constant c.

For the simulation of magnetic noise, we obtain τ using the spectral density measurement provided by the experimental group of Wunderlich at Siegen (Baumgart and Wunderlich [2013]). Figure 6.2 plots the measurement in log-log coordinates, displaying an overall shape consistent with the Ornstein-Uhlenbeck model (smooth curve with a turning point) (Gillespie [1996b]). The turning point of the graph yields an estimate of $\tau = 0.1$ ms. An estimate of c is obtained by calibrating to the lifetime of the $|D\rangle$ state

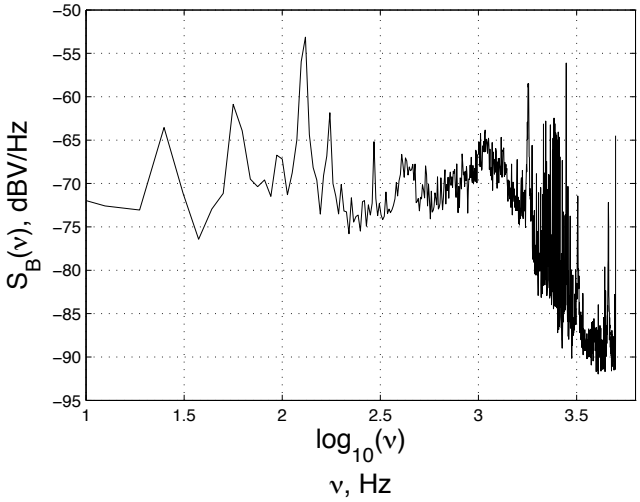

Figure 6.2: Antenna measurement of the (unnormalised) spectral density function of magnetic noise in the laboratory setting (Baumgart and Wunderlich [2013]). Using $x = 3.2$ as the horizontal coordinate of the turning point yields $\tau = 0.1$ ms.

found in Timoney et al. [2011]. The term $\mu(t)$ in (6.6) is thus found to have an estimated (fully relaxed) standard deviation of $2\pi \cdot 88$ Hz.

Noise is added to the Rabi frequencies of the microwave and radio wave fields assuming the same relaxation time of 0.1 ms. An estimate for c is obtained by assuming noise standard deviation of 0.3%. In this chapter's notation, we have used the estimate $f = 0.003$ for the microwave noise (see (6.7, 6.8)). An analogous parameter $f_{rw} = 0.003$ is introduced for the radio frequency field.

The fidelity of a quantum state ρ, with respect to a desired target or comparison state $|\Psi_c\rangle$, is defined (Nielsen and Chuang [2010]):

$$F(|\Psi_c\rangle, \rho) = \sqrt{\langle \Psi_c | \rho | \Psi_c \rangle} \tag{6.41}$$

so that the probability of finding $|\Psi_c\rangle$ upon measurement is given by F^2. There is a square root difference between this definition and the convention used in the paper by Sørensen and Mølmer [2000].

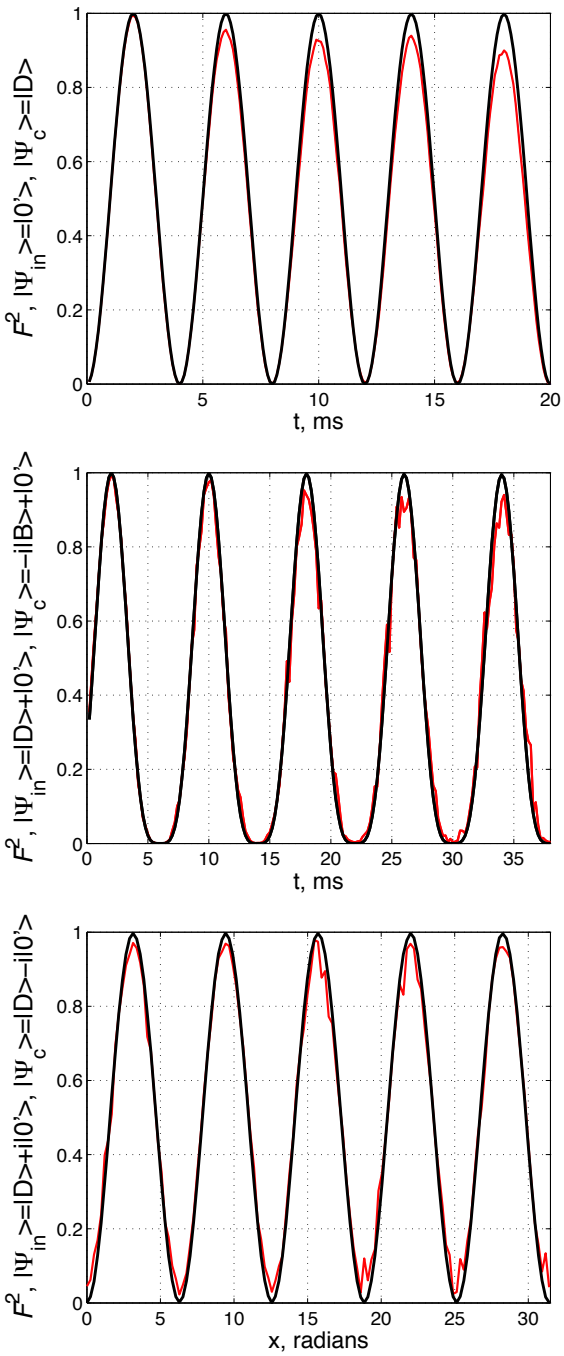

Figure 6.3: Simulation results for the single-qubit operations. The squared fidelity F^2 is plotted for each process, with the (unnormalised) input and comparison states shown. Results are obtained after averaging over 5 runs in each data set. TOP: Basic σ_y gate using $\Omega = 2\pi \cdot 40$ kHz (black), $2\pi \cdot 5$ kHz (red). Other parameters: ϕ_-= ϕ_+=1.57 rad, Ω_g=$2\pi \cdot 177$ Hz. MIDDLE: adiabatic transfer using $\Omega = 2\pi \cdot 40$ kHz (black), $2\pi \cdot 6$ kHz (red). Adiabatic rate is set to 1.57 rad/ms. BOTTOM: adiabatic σ_z gate using $\Omega = 2\pi \cdot 24$ kHz (black), $2\pi \cdot 103$ kHz (red). Adiabatic rate is set at 1.57 rad/ms, so each data point is reached in 2ms.

6.6.1 Basic σ_x/σ_y gates

Results for the basic σ_y gate are shown in Figure 6.3 top. Detailed simulation parameters are provided in the caption. The plot makes clear the efficiency of shielding against noise by means of the microwave dressing fields. At $\Omega = 2\pi \cdot 40$ kHz (the black curve), one obtains a reliable gate of almost vanishing noise contribution on the time scale considered. Averaging over 5 runs, the gate fidelity reaches $F = 99.9\%$ after the first 18ms. A reduction in Ω leads to the emergence of noise effects (the red curve), more than 98% of which are attributable to leakage into the $\{|u\rangle, |d\rangle\}$ states.

Further speed-up of the gate is possible by increase in the radio wave Rabi frequency, while maintaining the constraint for noise suppression (6.16). This requirement is far from exhausted with the present simulation parameters. On the other hand, slowing the gate down to the time-scale of hundreds of milliseconds yields lifetimes that are consistent with the findings by Timoney et al. [2011].

The gate is very robust against increased noise in the radio frequency field strength Ω_g, yielding fidelity above 99% at 18ms even with $f_{rw} = 0.1$ (using $\Omega = 2\pi \cdot 40$ kHz). An increase in the microwave noise to $f = 0.01$ is tolerable on the same criterion. In contrast, raising microwave noise to $f = 0.05$ yields a reduction to $F < 90\%$ at 18ms, which is uncorrectable even by raising Ω to $2\pi \cdot 300$ kHz.

6.6.2 Adiabatic transfer

Figure 6.3 middle shows the simulation results for adiabatic transfer using a superposition state. Again, $\Omega = 2\pi \cdot 40$ kHz is found to provide sufficient shielding on the timescale considered, yielding 99.9% fidelity after the first 18ms, using a simulation average of 5 runs. Reduction in Ω leads to increase in noise effects, more than 97% of which are found to take the form of leakage out of the qubit space.

Simulations suggest that reliable adiabatic following is maintained for the adiabatic rate $< \Omega/20$, so that speeding up of the process would eventually require an increase in the dressing field strength.

Simulations also suggest that $f = 0.01$ would represent a tolerable increase in microwave Rabi frequency noise, yielding fidelity $F > 99\%$ after

18ms ($\Omega = 2\pi \cdot 40$ kHz). On the other hand, setting $f = 0.05$ reduces the transfer fidelity below 90% at 18ms. This disturbance can not be corrected by raising Ω to $2\pi \cdot 318$ kHz.

6.6.3 Adiabatic σ_z gate

Figure 6.3 bottom panel displays results for the adiabatic σ_z gate. In contrast to the other quantum operations, we have plotted the angular parameter x (see Figure 6.1) on the horizontal axis, since reaching any x takes the same amount of time for this gate. This property is also visible in the absence of any noise evolution with increasing x.

The black curve illustrates a high-fidelity gate of 2ms duration (each point). As suggested in section 6.4, an optimum value for Ω is indeed found, below and above which the gate fidelity is reduced. In this instance, using $\Omega = 2\pi \cdot 24$ kHz yields the fidelity of 99.9%, averaging over 5 runs. Reducing Ω leads to increased noise effects in the form of leakage. In contrast, using increased Ω is found to reduce leakage effects but to introduce disturbances of non-leakage type (this case is plotted in Figure 6.3 red curve).

Reducing the gate duration via increased adiabatic rate, while keeping all other parameters constant, does appear to lead invariably to better fidelities for the σ_z gate. A limit on the gate speed is set by the adiabacity requirement, which is found to be: adiabatic rate $< \Omega/20$.

Retaining the gate duration of 2ms but increasing the microwave and radio wave Rabi frequency noise to $f, f_{rw} = 0.05$ leads to optimised fidelity with Ω in the vicinity of $2\pi \cdot 6$ kHz. Fidelities slightly above $F = 95\%$ are achieved. Setting $f, f_{rw} = 0.01$ enables one to reach fidelity above $F = 99\%$, with optimum field strength in the vicinity of $\Omega = 2\pi \cdot 11$ kHz.

6.7 The effect of magnetic gradient

The multi-qubit entangling gate presented in chapter 7 makes intrinsic use of static magnetic-field gradient being present along the trap axis. This is also likely to be the case, within the experimental context, for the single-qubit gates. However, introducing a magnetic-field gradient in the single-qubit analysis of the present chapter is not expected to add a significant

effect.

One can estimate analytically the magnitude of this contribution. Assuming a single motional mode only, the two phonon terms that would be added to the single-qubit Hamiltonian H (6.5) are:

$$H_p = \nu b^\dagger b + \kappa \sigma_z (b^\dagger + b) \tag{6.42}$$

(see (7.2)). No sideband coupling is employed for the single-qubit gates, and one can view the total Hamiltonian in the interaction picture with respect to $\nu b^\dagger b$. This leaves the terms in H unaffected. Evaluating the magnitude of $\kappa \sigma_z (b^\dagger + b)$ after the interaction picture, one recovers the following term in the second order:

$$H_{p2} = -\eta^2 \nu \ |D\rangle\langle D|. \tag{6.43}$$

This would amount to a tiny effect for realistic experimental parameters (7.28). The effect on this term of a further interaction picture with respect to the microwave energy gap of form $\Omega \left(|u\rangle\langle u| - |d\rangle\langle d| \right)$ can be neglected, provided that $\Omega \ll \nu$.

Numerical simulation of single-qubit gates with magnetic gradient present has also been carried out to establish that the gradient amounts to a negligible effect.

6.8 Summary

Two independent σ_i operations are required for the realisation of universal single-qubit dynamics, such that any point on the Bloch sphere can be reached. The simplest arrangement for the dressed-state qubit gate (section 6.2) enables only one σ_i gate to be realised for either of the B or the D-qubits, so that the need for complementary methods is raised.

As the simplest way to implement another σ_i operation, we propose the adiabatic transfer between the B and D-qubits in section 6.3, which is the next simplest operation to be realised experimentally and is found to possess good shielding properties. We also show how to realise a second independent gate, the σ_z gate, directly in sections 6.4 and 6.5. Of

these proposals, the design of section 6.5.2 to implement the σ_z gate using radio-wave Stark shift is expected to yield the gate with the best overall properties, however, it goes beyond the experimental limitations considered. The other σ_z gate designs can be looked at and considered in light of a particular experimental arrangement.

We will also consider, in sections 8.3 and 8.3.1, the possibility to go beyond the experimental limitations of the current chapter (to operate in the non-linear regime) and the implications of this for the single-qubit gate realisation. The added experimental facility enables the realisation of single-qubit gate schemes beyond the ones considered feasible in the present chapter. In particular, the basic gate arrangement of section 6.2 is now sufficient to realise two independent rotations for either the B or the D-qubits. Moreover, the σ_z gate of section 6.5.2 will also now be enabled. This provides the best recommendation for the non-linear regime, although many alternative designs would also exist to realise universal single-qubit rotations in this set-up.

Chapter 7

Multi-qubit gate

It is now shown how the dressed-state approach, combined with magnetic-gradient-induced coupling, enables the realisation of an entangling gate. We consider the additional effect of static magnetic-field gradient along the trap axis and show how a Hamiltonian of generalised Jaynes-Cummings form (Jaynes and Cummings [1963]) can be obtained. It is then used to construct the fast Mølmer-Sørensen gate (Sørensen and Mølmer [2000]).

Magnetic noise effects are discussed explicitly, demonstrating how microwave shielding can be accomplished. As the second key factor affecting the gate fidelity, we consider explicitly the effects of spurious couplings and resonances arising from the system Hamiltonian (7.1 - 7.2) as well as the presence of unused motional modes. Strategies for minimising these unwanted interactions are discussed. Further detrimental effects such as noise in the light field Rabi frequencies, effects due to stray addressing of individual particles in the frequency space, or known approximations of the trapped-ion physical system (James [1998]) could also be tackled in further research.

We derive and simulate an entangling gate for the two-particle case with the simplification of considering explicitly a single motional mode only. The issue of avoiding coupling to the other motional mode is discussed, as well as the scope for extending the discussion to the multi-particle case.

This chapter contains original research work, except where referenced otherwise. Both original theoretical calculations and simulations have been carried out to understand the workings of the proposed gate.

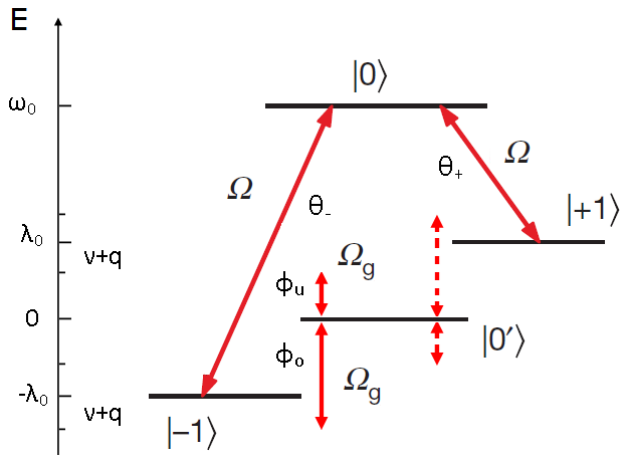

Figure 7.1: Realising the Mølmer-Sørensen gate. Two radio frequency fields (Rabi frequency Ω_g), detuned by $\pm q$ from the motional sidebands, generate four couplings between the states $|-1\rangle$, $|0'\rangle$, and $|1\rangle$. Microwave fields (Rabi frequency Ω) contribute to the shielding.

7.1 Set-up and definitions

Figure 7.1 depicts the arrangement for the gate implementation, together with definitions of the microwave and radio frequency fields. Two detuned radio frequency fields are employed, which generate four couplings in the $\{|-1\rangle, |0'\rangle, |+1\rangle\}$ triplet of states. The two microwave fields required will be shown to generate a shielding effect directly analogous to that in the single-qubit gates. The presence of the magnetic field gradient makes the energies of $|-1\rangle$ and $|+1\rangle$ position-dependent, so that λ_0 now represents the equilibrium value of $\lambda(z)$ for each trapped particle. Communication between individual qubits will be accomplished by means of a shared motional mode of the ions in the trap. We will present the derivations assuming the centre-of-mass mode plays the role of this 'bus qubit', denoting its frequency by ν. Section 4.4 and the preceding sections provide the other definitions used throughout this chapter.

7.2 Single-particle Hamiltonian

In the interaction picture with respect to $H_0 = \omega_0|0\rangle\langle 0| + \lambda_0|1\rangle\langle 1| - \lambda_0|-1\rangle\langle -1|$ and after performing the RWA, one obtains the following

Hamiltonian for the interactions depicted in Figure 7.1:

$$
\begin{aligned}
H = \; & \frac{\Omega}{2}\left(e^{-i\theta_-}|0\rangle\langle -1| + e^{-i\theta_+}|0\rangle\langle 1| + h.c.\right) + \\
& \frac{\Omega_g}{2}\left(e^{i(\nu+q)t}e^{-i\phi_u}|0'\rangle\langle -1| + e^{-i(\nu+q)t}e^{-i\phi_o}|0'\rangle\langle -1| + h.c.\right) + \\
& \frac{\Omega_g}{2}\left(e^{i(\nu+q)t}e^{-i\phi_u}|1\rangle\langle 0'| + e^{-i(\nu+q)t}e^{-i\phi_o}|1\rangle\langle 0'| + h.c.\right) \qquad (7.1) \\
& + \; \nu b^\dagger b + \kappa\tilde{\sigma}_z(b^\dagger + b). \qquad (7.2)
\end{aligned}
$$

The microwave and radio wave part (7.1) is directly analogous to the one previously quoted (6.5). Line (7.2) contains the phonon energy and the term due to the presence of the magnetic gradient (Mintert and Wunderlich [2001]).

As the next step, one applies the Schrieffer–Wolff transformation (Bravyi et al. [2011]) of form:

$$M \to e^{\tilde{\eta}\tilde{\sigma}_z(b^\dagger - b)} M e^{-\tilde{\eta}\tilde{\sigma}_z(b^\dagger - b)}. \qquad (7.3)$$

Its effect is to introduce factors to all terms in (7.1) as well as to remove the $\kappa\tilde{\sigma}_z(b^\dagger + b)$ contribution. The following additional term is obtained after the transformation:

$$H_{SW} = -\tilde{\eta}^2\nu\tilde{\sigma}_z^2. \qquad (7.4)$$

The factor $\tilde{\sigma}_z^2$ is not equal to the identity operator, since the Hilbert space contains four atomic levels, not two. Moving to the interaction picture with respect to the phonon term $\nu b^\dagger b$, one obtains from (7.1-7.2) the following

Hamiltonian:

$$
\begin{aligned}
H = \; & \frac{\Omega}{2}\left(e^{-i\theta_-}|0\rangle\langle -1|e^{\tilde{\eta}(\tilde{b}^\dagger - \tilde{b})} + h.c.\right) + \\
& \frac{\Omega}{2}\left(e^{-i\theta_+}|0\rangle\langle 1|e^{-\tilde{\eta}(\tilde{b}^\dagger - \tilde{b})} + h.c.\right) + \\
& \frac{\Omega_g}{2}\left(e^{i(\nu+q)t}e^{-i\phi_u}|0'\rangle\langle -1|e^{\tilde{\eta}(\tilde{b}^\dagger - \tilde{b})} + h.c.\right) + \\
& \frac{\Omega_g}{2}\left(e^{-i(\nu+q)t}e^{-i\phi_o}|0'\rangle\langle -1|e^{\tilde{\eta}(\tilde{b}^\dagger - \tilde{b})} + h.c.\right) + \\
& \frac{\Omega_g}{2}\left(e^{i(\nu+q)t}e^{-i\phi_u}|1\rangle\langle 0'|e^{\tilde{\eta}(\tilde{b}^\dagger - \tilde{b})} + h.c.\right) + \\
& \frac{\Omega_g}{2}\left(e^{-i(\nu+q)t}e^{-i\phi_o}|1\rangle\langle 0'|e^{\tilde{\eta}(\tilde{b}^\dagger - \tilde{b})} + h.c.\right) + \\
& H_{SW}. \qquad (7.5)
\end{aligned}
$$

7.3 Jaynes-Cummings-type coupling

The gate will be illustrated for the case of the D-qubit, noting that an analogous construction for the B-qubit is possible. One sets in (7.5):

$$
\begin{aligned}
\theta_- &= \theta_+ = 0 \\
\phi_u &= \phi_o = 0. \qquad (7.6)
\end{aligned}
$$

Expanding the coupling terms to first order in $\tilde{\eta}$ and changing basis to $\{|u\rangle, |d\rangle, |D\rangle, |0'\rangle\}$, one obtains:

$$
\begin{aligned}
H = \; & \frac{\Omega}{\sqrt{2}}\left(|u\rangle\langle u| - |d\rangle\langle d|\right) + & (7.7)\\
& \frac{\tilde{\eta}\Omega_g}{\sqrt{2}}\left(-e^{iqt}\,b \;+\; e^{-iqt}\,b^\dagger\right)|0'\rangle\langle D| \;+\; h.c. & (7.8)\\
& \frac{\tilde{\eta}\Omega_g}{\sqrt{2}}\left(-e^{-iqt-2i\nu t}\,b \;+\; e^{iqt+2i\nu t}\,b^\dagger\right)|0'\rangle\langle D| \;+\; h.c. & (7.9)\\
& \qquad + \; H_{res} \; + \; H_{SW}. & (7.10)
\end{aligned}
$$

Line (7.8) gives the sought-after Jaynes-Cummings type of coupling in

the qubit space (we refer to the contribution as Jaynes-Cummings 'type', since it contains counterrotating terms, which the regular Jaynes-Cummings Hamiltonian does not). The terms oscillating with frequency $\pm q$ will be used in building the entangling gate, while the effect of the faster-oscillating $\pm(q+2\nu)$ terms (7.9) will be minimised.

Line (7.7) is the energy gap created by the microwaves, analogous to the single-qubit case. H_{res} represents numerous residual terms that contain ν and q in their rotation frequencies. An expression for H_{res} in the interaction picture with respect to (7.7) is quoted:

$$\begin{aligned} H_{res} = \frac{1}{2}\Bigg(&\tilde{\eta}\Omega(-e^{it\nu - it\Omega/\sqrt{2}}b^\dagger + e^{-it\nu - it\Omega/\sqrt{2}}b)|D\rangle\langle u| + \\ &\Omega_g(e^{-itq - it\nu - it\Omega/\sqrt{2}} + e^{itq + it\nu - it\Omega/\sqrt{2}})|0'\rangle\langle u| + \\ &\tilde{\eta}\Omega(e^{it\nu + it\Omega/\sqrt{2}}b^\dagger - e^{-it\nu + it\Omega/\sqrt{2}}b)|D\rangle\langle d| + \\ &\Omega_g(e^{-itq - it\nu + it\Omega/\sqrt{2}} + e^{itq + it\nu + it\Omega/\sqrt{2}})|0'\rangle\langle d| \\ &+ h.c.\Bigg) \end{aligned} \tag{7.11}$$

These terms would be expected to cancel by rotating wave arguments, however, they will be shown to contribute to two distinct spurious coupling effects.

Considering the effect of magnetic noise in the dressed basis, the following contribution is found:

$$H_n = -\frac{\mu}{\sqrt{2}}\left(|D\rangle\langle u| + |D\rangle\langle d| + h.c.\right). \tag{7.12}$$

This can be compared to (6.13). Moving to the interaction picture with respect to (7.7) will generate shielding against magnetic noise, as has been presented before. This mechanism is maintained, as one extends the discussion to multi-particle Hamiltonians.

7.4 Derivation summary

The single-particle derivation given in the previous two sections, along with the introduction of the effective Lamb-Dicke parameter, can be compared

to the derivation given in section 5.4. The points below summarise the key differences between the two:

- Some notational difference. ε_c is introduced in (5.19) while κ is being used in (7.2). The two definitions are consistent.

- Different sequence of steps. The interaction picture with respect to the phonon term $\nu b^\dagger b$ is applied at different stages. Also, the interaction picture with respect to the energy level height and the corresponding RWA are taken at different stages in the two derivations.

- The conventional Lamb-Dicke parameter is essentially zero in the derivation of the present chapter. Therefore, no necessity to invoke the γ parameter (5.54).

- The couplings for the Hamiltonian derived in the present chapter are always between a magnetically sensitive and a magnetically insensitive state (see Figure 7.1). This has the effect of reducing the effective Lamb-Dicke parameter by 1/2 compared to the treatment in section 5.4 (and assuming zero conventional Lamb-Dicke parameter there). This is reflected in the definitions specified (see (4.7)).

- The Hilbert space in the present chapter consists of four states, so that the identity $\tilde{\sigma}_z^2 = 1$ no longer holds. This results in the introduction of H_{SW} (7.4).

- A change of basis is involved in the present chapter, since it is of interest to couple dressed states. There is also the resultant H_{res} term (7.11).

- In section 5.4, Jaynes-Cummings form is recovered only after the second RWA, once the detuning is fixed in (5.53) (after expanding $\tilde{\eta}$ to first order). In contrast, no second RWA is needed in this chapter's derivation. Having one less approximation within the derivation makes the experimental parameter constraints slightly less stringent, as well as removes a source of potential deviation.

7.5 Two-particle Hamiltonian

We present and simulate the entangling gate for the two-particle case, noting that a multi-particle entangling gate would also be viable. The case discussed is for the D-qubit, using the centre-of-mass mode. The breathing mode is not treated explicitly, but the effects of its presence will be discussed in section 7.7.

The single-particle Hamiltonian (7.7-7.10) needs to be rederived for the extended $(\mathcal{H}_{ion1} \otimes \mathcal{H}_{ion2}) \otimes \mathcal{H}_{phonon}$ Hilbert space, making the necessary modifications. The term $\kappa\tilde{\sigma}_z(b^\dagger + b)$ in line (7.2) enters with the same sign for each of the two qubits, provided that the centre-of-mass mode is assumed. One performs the Schrieffer–Wolff transformation of form:

$$M \to e^{\tilde{\eta}(\tilde{\sigma}_{z1}+\tilde{\sigma}_{z2})(b^\dagger - b)} M e^{-\tilde{\eta}(\tilde{\sigma}_{z1}+\tilde{\sigma}_{z2})(b^\dagger - b)} \tag{7.13}$$

to remove the $\kappa\tilde{\sigma}_{zi}(b^\dagger + b)$ contributions and recover the following extra term:

$$H_{SW2} = -\tilde{\eta}^2\nu\ (\tilde{\sigma}_{z1} + \tilde{\sigma}_{z2})^2. \tag{7.14}$$

The other steps in the derivation (interaction picture, rotating wave approximation, basis change) are generalised straightforwardly to the two-qubit case to yield a generalisation of the Hamiltonian (7.7-7.10). Finally, one moves to the interaction picture with respect to the (generalised version of) microwave part (7.7) to obtain the two-qubit Hamiltonian of the final form. This step leaves the terms (7.8-7.9) unaffected.

Using the definition:

$$\tilde{\sigma}_+ = |D\rangle\langle 0'| \tag{7.15}$$

the Jaynes-Cummings-type terms ((7.8), in the extended Hilbert space) can be rewritten in the form:

$$H_q = i\frac{\tilde{\eta}\Omega_g}{\sqrt{2}}\left(\tilde{\sigma}_{y1} + \tilde{\sigma}_{y2}\right)\left(e^{iqt}b - e^{-iqt}b^\dagger\right). \tag{7.16}$$

This expression is used to obtain the fast Mølmer-Sørensen gate.

The effect of the faster-oscillating terms of form (7.9) (in the extended space) will be minimised by parameter choice. One checks for any other unwanted interactions in the final Hamiltonian by expanding it to the second order in the Dyson series and looking for secular terms. The following additional contribution is found:

$$H_{add} \; =$$

$$\frac{-2\tilde{\eta}^2\nu^3}{2\nu^2-\Omega^2}\cdot\Big(2|DD\rangle\langle DD| + |D0'\rangle\langle D0'| + |0'D\rangle\langle 0'D| + |DD\rangle\langle ud| + |DD\rangle\langle du| + |ud\rangle\langle DD| + |du\rangle\langle DD|\Big) \tag{7.17}$$

which affects significantly the gate performance and needs to be minimised.

7.6 Fast entangling gate

Following the proposal of Sørensen and Mølmer [2000], a two-qubit entangling gate can be obtained from the Hamiltonian H_q (7.16). The functions $F(t)$ and $G(t)$ (defined in the Mølmer-Sørensen derivation) need to be set to zero, which imposes the constraint:

$$qt = 2\pi \cdot R \tag{7.18}$$

for integer R. Setting in addition:

$$t\frac{\tilde{\eta}^2\Omega_g^2}{q} = \frac{\pi}{4} \tag{7.19}$$

leads to the desired unitary evolution, which generates entanglement between the qubits:

$$U_T = \mathrm{Exp}\Big(\frac{-i\pi}{4}\cdot(1+\tilde{\sigma}_{y1}\tilde{\sigma}_{y2})\Big). \tag{7.20}$$

Given a value for R, the conditions (7.18, 7.19) fix the time of the

entanglement operation to:

$$T = \frac{\pi\sqrt{R}}{\sqrt{2}\tilde{\eta}\Omega_g}. \tag{7.21}$$

Furthermore, the value for q is also determined:

$$q = 2\sqrt{2R}\tilde{\eta}\Omega_g. \tag{7.22}$$

7.7 Minimising spurious couplings

Experimental parameters have to be chosen to minimise excitations of the other motional mode and the effect of the resonance term (7.17). The breathing mode frequency is given by $\nu' = \sqrt{3}\nu$ (which is also the next lowest frequency in the N-particle case (Šašura and Bužek [2002])), and the introduction of the breathing mode phonon terms $\nu' b'^{\dagger} b'$ and $\pm\kappa'\tilde{\sigma}_z(b'^{\dagger} + b')$ in the Hamiltonian (see (7.2)) would lead to extra prefactors of form $e^{\pm\tilde{\eta}'(\tilde{b'}^{\dagger} - \tilde{b'})}$ in (7.5).

Considering the effect of such terms on the qubit-space couplings (7.8, 7.9), the next lowest oscillation frequency after $e^{\pm iqt}$ will be close to $e^{\pm i(\nu-\nu')t}$ (assuming $q \ll \nu$). It will be found in terms of the following functional form:

$$\frac{\tilde{\eta}'\Omega_g}{\sqrt{2}} e^{i(\nu-\nu')t}\ b' \approx \frac{\tilde{\eta}\Omega_g}{3.25}\ e^{-i\cdot 0.73\nu t}\ b' \tag{7.23}$$

where we have used $\nu' = \sqrt{3}\,\nu$ and $\tilde{\eta}' = 3^{-3/4}\,\tilde{\eta}$ (see (4.7) and above). This represents the effect to be minimised, which generates a term in the second order of the Dyson series. Comparing this coupling with the strength of the gate coupling (7.21) leads to the condition:

$$\begin{aligned} \frac{\tilde{\eta}^2\Omega_g^2}{\nu} &\ll \tilde{\eta}\Omega_g \\ \tilde{\eta}\Omega_g &\ll \nu. \end{aligned} \tag{7.24}$$

This constraint also ensures that the terms (7.9) yield a negligible effect.

Secondly, the magnitude of the terms in (7.17) can be minimised (using

the assumption $\nu^2 \gg \Omega^2$) by requiring the following:

$$\tilde{\eta}^2 \nu \ll \tilde{\eta}\Omega_g$$
$$\tilde{\eta}\nu \ll \Omega_g. \tag{7.25}$$

Conditions (7.24) and (7.25), together with the expressions for T and q (7.21, 7.22) and the relationship $\tilde{\eta} \propto \nu^{-3/2}$ constrain the choice of experimental parameters and ultimately the properties of the entangling gate that can be produced within a given set of experimental constraints. A good range of suitable parameters can still be found within reach of the current experimental capabilities ((7.28) provides an example).

The presence of a further motional mode in the derivation would also modify the expressions for H_{SW2} (7.14) and H_{res} (7.10), which would mathematically alter the unwanted resonance effects to some degree. This modification, which in general would depend on the particle number, can be tackled further by analytical and numerical techniques.

7.8 Fidelity correction

A third prominent unwanted coupling effect is found in numerical simulation and can be traced to terms in H_{res}, specifically, the part proportional to Ω_g (see (7.11)). The effect of these terms is to superimpose a fast-oscillating time dependence on some of the plots for state fidelity during the gate operation.

The analytical treatment of this effect mirrors closely the derivation by Sørensen and Mølmer [2000] (section III A. Direct coupling). Firstly, we assume $\Omega \ll q + \nu$, so that the terms responsible for the disturbance can be approximated to the following expression (here quoted for the single-particle Hamiltonian):

$$H_{c:1q} = \frac{\Omega_g}{2}\Big((e^{-itq-it\nu} + e^{itq+it\nu})|0'\rangle\langle u| + (e^{-itq-it\nu} + e^{itq+it\nu})|0'\rangle\langle d| + h.c.\Big). \tag{7.26}$$

Secondly, taking the desired gate evolution to be $U(t)$, one transforms the disturbance (rewritten for the two-qubit case) to the interaction picture: $H_{cI}(t) = U^{\dagger}(t)H_c(t)U(t)$, and considers expanding $H_{cI}(t)$ in the Dyson series to evaluate the magnitude of the disturbance.

Two simplifying approximations are made. Firstly, $U(t)$ is taken to be slowly-varying in comparison to $H_c(t)$, so that it can be regarded as constant when performing the Dyson series integrals. Secondly $H_{cI}(t)$ is evaluated in the vicinity of the endpoint of the gate operation ($t = T$), where $U(t)$ takes a simple form (7.20) and is approximated to be time-independent.

Obtaining an expression for $H_{cI}(t)$ in such a manner to the second order in the Dyson series, one can calculate the fidelity of certain output states, given a particular input state. One also needs to account for the fact that an interaction picture has been adopted. Again, we use a different definition of fidelity to the paper by Mølmer and Sørensen: $F(|\Psi_c\rangle, \rho) = \sqrt{\langle\Psi_c|\rho|\Psi_c\rangle}$ (see (6.41)), so that state probabilities are given by F^2.

Beginning in the state $|DD\rangle$ and calculating the fidelity of $|DD\rangle$ at the end of the gate operation, one recovers $F^2 = \frac{1}{2}$. This is consistent with the unitary gate evolution (7.20) and is verified in the numerical simulation (see Figure 7.2 top), where no oscillatory effect is observed. In contrast, starting in the state $|DD\rangle$ and calculating the fidelity of $\frac{1}{\sqrt{2}}(|DD\rangle + i|0'0'\rangle)$, the following is obtained:

$$F^2 = 1 - \frac{2\Omega_g^2}{(q+\nu)^2}(\sin{(q+\nu)t})^2 + \mathcal{O}\left(\frac{\Omega_g^4}{(q+\nu)^4}\right). \tag{7.27}$$

An oscillatory correction is thus introduced to the fidelity of the entanglement operation. Numerical simulation suggests that (7.27) predicts very accurately the frequency and the amplitude of the oscillations observed (see Figure 7.2 bottom). A simliar calculation can be carried out for any other input and comparison states.

This oscillatory effect can be minimised by reducing Ω_g/ν, or by adjusting precisely the gate duration. Higher trap frequency ν will lead to a greater accuracy requirement for the length of the gate pulse.

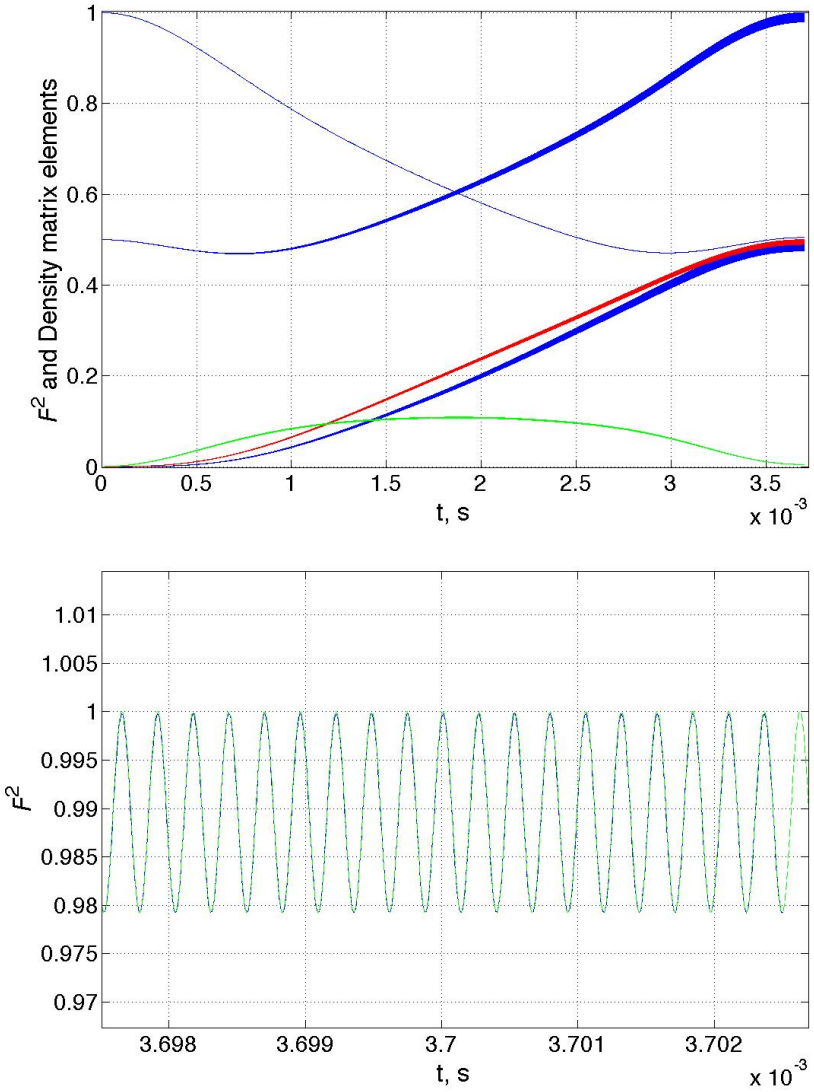

Figure 7.2: Simulation results for the two-qubit gate (Cohen [2014]). TOP: Squared fidelity and other density matrix elements for the two-qubit entangling gate. An input state of $|DD\rangle$ is used, and the simulation parameters are specified in (7.28). The first curve (counting from above at $t \approx 1.6$ ms) represents the squared fidelity of $|DD\rangle$, where no oscillatory component is found. The second curve is the squared fidelity of $\frac{1}{\sqrt{2}}(|DD\rangle + i|0'0'\rangle)$. The third is the imaginary part of $\rho_{|DD\rangle,|0'0'\rangle}$, the fourth is the squared fidelity of $|0'0'\rangle$, and the last curve is the real part of $\rho_{|DD\rangle,|0'0'\rangle}$. BOTTOM: A magnified segment of the squared fidelity plot of $\frac{1}{\sqrt{2}}(|DD\rangle + i|0'0'\rangle)$ from the figure above. The result of the calculation (7.27) is plotted superimposed.

7.9 Simulation

Numerical simulation of the two-qubit entangling gate is carried out to demonstrate its feasibility. We simulate a Hamiltonian of the form (7.1-7.2), extended to the two-qubit case. A single motional mode is used, which is chosen to be the centre-of-mass mode. The effects of magnetic noise in the multi-qubit case have been shown to be directly analogous to the single-qubit arrangement (see (7.12)), where sufficiently strong microwave dressing field renders the disturbance negligible. No magnetic noise or any other random noise effects have been included in the present simulation.

The following parameters are used:

$$\begin{aligned} \Omega &= 2\pi \cdot 40\,\mathrm{kHz} \\ \Omega_g &= 2\pi \cdot 194\,\mathrm{kHz} \\ \tilde{\eta} &= 4.9 \cdot 10^{-4} \\ \nu &= 2\pi \cdot 1.9\,\mathrm{MHz} \\ n &= 0 \\ R &= 1. \end{aligned} \tag{7.28}$$

This parameter choice yields the gate time $T = 3.7$ ms, and sideband detuning $q = 2\pi \cdot 270$ Hz. The constant of proportionality linking ν and $\tilde{\eta}$ (see (4.7) and above) is obtained for the $^{171}Yb^{+}$ ion and magnetic gradient of 24 T/m. This represents well the current experimental capability in terms of gradients attainable in the laboratory (Hensinger [2014]). The most challenging aspect from an experimental point of view would be the precise sideband detuning q, which imposes a tight constraint on the permissible error for the trap frequency ν.

Figure 7.2 plots squared state fidelities and density matrix elements for the duration of the gate operation. An input state of $|DD\rangle$ has been used. The figure gives clear evidence for the feasibility of the entangling gate. Also, the oscillatory correction to the fidelity of the target state $\frac{1}{\sqrt{2}}(|DD\rangle + i|0'0'\rangle)$ is found to be in very good agreement with the mathematical description (7.27), as illustrated in the bottom panel. It is suggested that the best progress towards further improvements in the gate properties and the attainment of an optimum set of parameters would be

made in conjunction with a particular experimental group.

We have conducted the above simulation using the phonon ground state $|n = 0\rangle$, corresponding to absolute zero temperature. We have also examined simulation results with the initial state replaced with the $|n = 5\rangle$ and $|n = 10\rangle$ Fock states, finding an insignificant drop in fidelity. This is in good agreement with the known properties of the Mølmer-Sørensen gate, where coupling strengths remain independent of n. Such a property is crucial in shielding the gate against heating effects, whereby the phonon state inevitably suffers from the effects of thermalisation.

For any non-zero temperature, the phonons would become Planck-distributed, so that the proper description of the phonon state would be the thermal state: a probabilistic mixture of Fock states $|n\rangle$ with n following the Planck distribution (Terzi [1998]). The mean phonon number $\bar{n}$ is linked to the equilibrium temperature T by the relation:

$$\bar{n} = \frac{1}{e^{\frac{\hbar\nu}{k_B T}} - 1} \approx \frac{k_B T}{\hbar\nu} \tag{7.29}$$

where k_B is the Boltzmann constant (Wineland et al. [1997]). Considering the phonon frequency ν used in the simulation, $\bar{n} = 10$ would correspond to $T \approx 1$ mK.

Our preliminary simulations using simple Fock states would suggest the gate developed to be stable against heating up to this temperature. More elaborate computational models to study heating effects (Sørensen and Mølmer [1999]; Wineland et al. [1997]) can also be developed to study further the gate properties, taking also into consideration a particular heating rate.

Chapter 8

Beyond the linear regime

This chapter briefly discusses extensions and generalisations of the dressed-state approach to the regime where non-linear energy level shift plays a prominent role. The case of $^{171}Yb^{+}$ is discussed in particular. We delineate precisely the 'linear' regime for this physical system, which is the region of validity for the derivations presented in chapters 6 and 7. We also define and discuss a 'non-linear' regime, exemplified by the recent work of Webster et al. [2013]. The relative merits of these two parameter ranges are then considered, together with a possible strategy for attaining either experimentally by means of microwave dressing fields.

This chapter is original research work, except where referenced otherwise.

8.1 Hyperfine Zeeman shift in $^{171}Yb^{+}$

The four-level system depicted in Figure 5.3 can be realised using the $F = \{0, 1\}$ hyperfine ground state of $^{171}Yb^{+}$ with non-zero external magnetic field. The $|1\rangle$ and $|-1\rangle$ states would correspond to the $m_f = \pm 1$ levels of the $F = 1$ triplet, $F = 1, m_f = 0$ level would yield the $|0'\rangle$ state and $|0\rangle$ would be represented by the singlet $F = 0$ state (see section 2.4). The study by Blatt et al. [1983] presents a detailed energy-level diagram of the system as well as provides an accurate measurement of the singlet-triplet energy splitting, which is approximately $A = 2\pi \cdot 12.6$ GHz.

As described in section 2.4, the $|\pm 1\rangle$ states would respond exactly

linearly to external magnetic field B, with a change in energy of $\pm\mu_B B$. The response of $|0'\rangle$ and $|0\rangle$ can be approximated to the lowest order by $\pm(\mu_B B)^2/A$ (Foot [2004]). For any non-zero external field, there is therefore an inevitable discrepancy between the $|-1\rangle \leftrightarrow |0'\rangle$ and $|0'\rangle \leftrightarrow |1\rangle$ resonant frequencies, which can be well approximated by the (positive) figure:

$$\Delta = \frac{2(\mu_B B)^2}{A}. \tag{8.1}$$

This enables the explicit definition of two simplified physical regimes.

8.2 Linear regime

The gates presented in the previous chapters are built on the assumption of negligible Δ, so that addressing of both $|-1\rangle \leftrightarrow |0'\rangle$ and $|0'\rangle \leftrightarrow |1\rangle$ pairs can be achieved by the same Ω_g field. Addressing one pair of levels exactly on resonance would mean that the other pair is addressed with the (positive) detuning equal to Δ. It is necessary to preserve this second coupling as a desired effect, with the contribution due to Δ being negligible.

In the single-qubit case, considering the Rabi model (Gerry and Knight [2005]), making the two interactions equivalent would require:

$$\begin{aligned} &\Omega_g \approx \sqrt{\Omega_g^2 + \Delta^2} \\ &\Omega_g^2 \gg \Delta^2. \end{aligned} \tag{8.2}$$

In the multi-qubit case, where the gate interaction strength is of the order $\eta\Omega_g$, one requires Δ to obey the following constraint:

$$\eta\Omega_g \gg \Delta. \tag{8.3}$$

In both cases, an upper limit on the permissible magnetic field is placed by the strength of the RF fields employed.

In the chapters above, we have also assumed that magnetic noise affects prominently the $\{|-1\rangle, |1\rangle\}$ states, but negligibly the $\{|0\rangle, |0'\rangle\}$ pair of levels. This relies on the assumption of small magnetic field. Comparing the sensitivity of $|\pm 1\rangle$ to magnetic noise with the (B-field dependent)

sensitivity of $|0'\rangle$ leads to the requirement:

$$B \ll 0.45 \text{ T}. \tag{8.4}$$

8.3 Non-linear regime

This regime is defined as the instance when both $|-1\rangle \leftrightarrow |0'\rangle$ and $|0'\rangle \leftrightarrow |1\rangle$ pairs can be unambiguously individually addressed, without affecting the other coupling. In this case, the coupling of the other pair, with the detuning equal to Δ, would represent an unwanted effect to be made negligible. This is the case for prominent Δ, such that the Stark shift approximation (see section 2.1.3) applies. The condition is:

$$\Omega_g \ll \Delta \tag{8.5}$$

which also ensures that the magnitude of the energy shift of $|0'\rangle$, $\Omega_g^2/4\Delta$, is small compared to its Zeeman response, $\Delta/2$, and therefore amounts to a negligible effect.

Experiments within the non-linear regime have been conducted by Webster et al. [2013], also citing the condition (8.5). A field of 9.8 G is used to generate a measured frequency discrepancy $\Delta = 2\pi \cdot 29(1)$ kHz in agreement with (8.1). Radio frequency fields of strength $\Omega_g = 2\pi \cdot 1.9$ kHz have been employed.

The authors have discussed how the non-linear regime enables the realisation of arbitrary single-qubit σ_ϕ gates using a single radio frequency field. Also, the authors note that a σ_z gate could be realised by the use of a single detuned RF field.

The facility of individual addressing does offer clear experimental advantages, however, it may also be the case that greater sensitivity to magnetic noise is introduced as well. Considering the criteria (8.2, 8.5), it is probable that the non-linear regime will involve stronger B-fields than the linear regime, particularly for the arrangement of an ion chain. If the condition (8.4) is broken, this would introduce non-negligible noise in the energy of $|0'\rangle$, which is not shielded against in the present set-up.

A further problem for the non-linear arrangement might arise in the

attainment of individual addressing in an ion chain, due to the non-linear dependence of the energy spacings for individual qubits.

8.3.1 Single-qubit gates

A variety of ways to realise universal single-qubit rotations is possible in the non-linear regime. In addition to the proposals by Webster et al. [2013], it is noted that individual addressing ($\phi_- \neq \phi_+$) allows for the basic gate arrangement (section 6.2) to yield both the σ_x and the σ_y gates for the B and D-qubits. An extra error source to consider would be the instability of the radio frequency fields ($\delta_{\Omega g} = \Omega_{g-} - \Omega_{g+}$), due to two fields being necessary.

No extra effort would be required to realise adiabatic transfer, and the adiabatic σ_z gate (section 6.4) would be realisable by the usage of two RF fields per trapped particle. Further, the two σ_z gates presented in sections 6.5.1 and 6.5.2 are also a feasible alternative. In every case where two RF fields are being used, the small extra noise contribution due to $\delta_{\Omega g}$ would need to be considered.

8.3.2 Multi-qubit gate

The linear response of $|-1\rangle$ and $|1\rangle$ to magnetic field in the Ytterbium system permits the realisation of magnetic-gradient-induced coupling for any strength of the B-field, which is a crucial ingredient for the entangling gate. The reproduction of the Mølmer-Sørensen gate presented previously (chapter 7) would be possible in the non-linear regime by the usage of four radio frequency fields per trapped particle.

Separate RF addressing of the magnetic-sensitive states is found to offer no clear mathematical advantage in the construction of the entangling gate. It is possible to employ two radio frequency fields (in two arrangements) and reach an entangling Hamiltonian of form similar to (7.7-7.10). However, the speed of the resultant gate is reduced by 1/2.

Moreover, it is the property of the linear regime multi-qubit gate that the zeroth order in η is canceled within the qubit space, in the dressed basis, leaving only terms to the first order in η (see (7.8-7.9)). This property ceases to hold for a gate that is built using two RF couplings per trapped

particle. As a result, unwanted zeroth order terms of form $\Omega_g e^{\pm i(q+\nu)t}$ are introduced within the qubit space. This would lead to a more demanding set of constraints on the gate parameters.

These considerations make the Mølmer-Sørensen gate harder to realise in the non-linear regime.

8.4 Mediating technique

The linear and non-linear regimes are compounded by an intermediate region where neither perfect individual nor perfect mutual addressing in the qubit space are possible. The facility to reach either regime can be hampered by the existence of an upper limit on the B-field strength (8.4), as well as experimental limitations on the gate time or Ω_g. In such cases, an intermediate regime may be inevitable, with the ensuing presence of spurious couplings within the qubit space.

As an alternative to tackling explicitly such couplings, the technique of dressed Stark shift (section 6.5.1) offers a way of tuning Δ by means of microwave fields. Such a process would potentially provide easy mediation between the linear and non-linear regimes. Using a detuned microwave field specified by Ω_z, δ_z to induce a $|0\rangle \leftrightarrow |0'\rangle$ coupling together with the two microwave dressing fields leads to the following additional term in Δ:

$$\Delta = \frac{2(\mu_B B)^2}{A} + \frac{\delta_z \Omega_z^2}{\Omega^2 - 2\delta_z^2} \tag{8.6}$$

subject to the conditions for fast oscillation (6.36). This suggests the possibility of tuning Δ with the help of a second physical process. The above result is found by considering Ω_z and two microwave dressing fields only, so the potential cross-couplings due to the presence of RF fields would also need to be examined.

Within an ion chain, it is likely that a single Ω_z field would generate couplings between the $|0\rangle$ and $|0'\rangle$ states of all the ions involved, so that no individual control over δ_z and Ω_z would be attainable. However, independent tuning of Δ would still be possible, in principle, by means of the Ω dressing fields, which are well separated in frequency space.

Provided that the tuning of Δ can be realised with attainable experi-

mental parameters, dressed Stark shift offers a way of realising both linear and non-linear regimes using modest magnetic field strength. This would be of advantage for both single and multi-qubit designs.

Conclusion

The present dissertation has demonstrated the feasibility of universal quantum computation using microwave-dressed states in trapped ions or any other suitable system where magnetic-gradient-induced coupling can be utilised. Motivated primarily by the desire to apply long-wavelength radiation for trapped-ion quantum information processing, the key research problem addressed in the present research has been whether or not a universal set of gates could be build using superposition states, or dressed states, in the construction of the logical qubit. The idea of dressed states had been proposed and experimentally tested (Timoney et al. [2011]) to demonstrate its advantageous shielding qualities against magnetic noise. Also, elementary single-qubit operations had already been proposed (Timoney et al. [2011]; Webster et al. [2013]).

After presenting the relevant theoretical and experimental background material in the opening chapters, we have introduced and motivated the dressed-state approach and the usage of long-wavelength radiation together with the application of a static magnetic gradient. The traditional trapped-ion set-up has been first presented and comparisons with the new design drawn. We then proceed to explore the possibility of building quantum gates within the new design. Both original single and multi-qubit quantum gate operations have been proposed. Moreover, we have analysed in detail the key noise sources and criteria for their suppression in the laboratory setting, also demonstrating the attainment of high fidelity in the numerical simulations performed taking into account the key noise sources.

For the single-qubit case, we have proposed the operation of adiabatic transfer and developed an adiabatic σ_z gate. We have also analysed in detail the effects of magnetic and Rabi-frequency noise on the gate operations, including the original single-qubit gate proposed by Timoney et al. [2011].

Both analytical and simulations-based work have been carried out, and we cite the experimental criteria necessary for noise suppression. Various additional original single-qubit σ_z gate designs based on the effect of Stark shift and adiabatic following have also been proposed. We have commented on and clearly delineated the further experimental possibilities within the regime of non-linear magnetic response of the energy levels, first explored by Webster et al. [2013]. We have elaborated on the single-qubit gate operations possible within this regime, suggesting new possibilities and commenting on the potential challenges.

For the multi-qubit case, we have built an entangling gate based on the design of Mølmer and Sørensen. We have derived in detail the gate Hamiltonian and discussed the potential for extending the entangling operation to more than two particles. As the key factor of noise, we have analysed the effects of unwanted couplings and resonances, citing criteria for their minimisation. Because of the usage of the dressed-state approach, the gate has also been found to be robust against the effects of magnetic noise. We have carried out numerical simulation of the proposed design, giving a first indication for the experimental parameters necessary for the attainment of good gate fidelities. We have also commented on the possibility of realising the gate within the non-linear regime, finding this set-up less advantageous.

Finally, a new experimental technique has been proposed as a way of mediation between the linear and the non-linear regimes. Normally, the two regimes are delineated by the strengths of the ambient magnetic field and the radio wave Rabi frequencies used for the gates. With the added experimental technique of dressed Stark shift, a further pair of microwave coupling parameters is introduced into the equations, making the linear and non-linear regimes dependent on another independent physical process, which is accessible experimentally. This has the potential of easing the experimental challenges involved in the realisation of the quantum gates proposed.

The outcome of the research presented is to raise the prospects of long-wavelength-driven quantum computation as an exciting venue for future research. Experimental work towards the realisation of the proposed techniques would be keenly encouraged. An interesting theoretical question to address would be the implementability of other entangling gate designs

within the dressed-state system, possibly via adiabatic techniques. Also, it is of interest to explore further the properties of the proposed entangling gate within the regime of more that two particles or in the context of concrete experimental limitations and possibilities.

The key original contributions of the thesis are: section 5.4, which retraces the steps of a previous derivation to amend omissions. The two-level Hamiltonian for the magnetic gradient set-up has been re-derived, making explicit all the steps and approximations. Chapter 6 proposes and analyses in detail novel single-qubit operations and comments on those previously proposed. Noise analysis and simulations of the proposed schemes are carried out. Chapter 7 proposes, derives in detail and tests numerically a novel entangling gate for the dressed-state setting. We comment on the possibility for extending the design from two to multiple particles as well as present the key factors affecting the gate fidelity. Finally, chapter 8 places the gates in a clearer experimental context and suggests a novel experimental technique with the potential to ease the implementation of both single-qubit and multi-qubit gates within the laboratory setting.

References

Aharonov, Y. and Anandan, J. (1987). Phase change during a cyclic quantum evolution. *Physical Review Letters*, 58(16):1593. 21

Allen, L. and Eberly, J. (1987). *Optical Resonance and Two-Level Atoms*. Dover Publications. 18, 25

Barrett, M. D., Chiaverini, J., Schaetz, T., Britton, J., Itano, W. M., Jost, J. D., Knill, E., Langer, C., Leibfried, D., Ozeri, R., et al. (2004). Deterministic quantum teleportation of atomic qubits. *Nature*, 429(6993):737–739. 10

Baumgart, I. and Wunderlich, C. (2013). *personal communication*. 71, 72

Bergmann, K., Theuer, H., and Shore, B. W. (1998). Coherent population transfer among quantum states of atoms and molecules. *Reviews of Modern Physics*, 70(3):1003. 24, 25

Bermudez, A., Jelezko, F., Plenio, M. B., and Retzker, A. (2011). Electron-mediated nuclear-spin interactions between distant nitrogen-vacancy centers. *Physical Review Letters*, 107(15):150503. 54

Bermudez, A., Schmidt, P. O., Plenio, M. B., and Retzker, A. (2012). Robust trapped-ion quantum logic gates by continuous dynamical decoupling. *Physical Review A*, 85:040302. 54

Blatt, R., Schnatz, H., and Werth, G. (1983). Precise determination of the $^{171}yb^{+}$ ground state hyperfine separation. *Zeitschrift für Physik A Atoms and Nuclei*, 312(3):143–147. 23, 92

Blatt, R. and Wineland, D. (2008). Entangled states of trapped atomic ions. *Nature*, 453(7198):1008–1015. 10, 45

Bravyi, S., DiVincenzo, D. P., and Loss, D. (2011). Schrieffer–wolff transformation for quantum many-body systems. *Annals of Physics*, 326(10):2793–2826. 47, 80

Cai, J., Jelezko, F., Katz, N., Retzker, A., and Plenio, M. B. (2012a). Long-lived driven solid-state quantum memory. *New Journal of Physics*, 14(9):093030. 54

Cai, J., Jelezko, F., Plenio, M. B., and Retzker, A. (2013). Diamond-based single-molecule magnetic resonance spectroscopy. *New Journal of Physics*, 15(1):013020. 54

Cai, J., Naydenov, B., Pfeiffer, R., McGuinness, L. P., Jahnke, K. D., Jelezko, F., Plenio, M. B., and Retzker, A. (2012b). Robust dynamical decoupling with concatenated continuous driving. *New Journal of Physics*, 14(11):113023. 54

Cirac, J., Zoller, P., et al. (1995). Quantum computations with cold trapped ions. *Physical Review Letters*, 74(20):4091–4094. 9, 11, 41

Cohen, I. (2014). *personal communication*. 89

Cohen-Tannoudji, C., Diu, B., and Laloë, F. (2006). Quantum mechanics, 2 volume set. 19, 20

Danileiko, M. V., Romanenko, V. I., and Yatsenko, L. P. (1994). Landau-zener transitions and population transfer in a three-level system driven by two delayed laser pulses. *Optics communications*, 109(5-6):462–466. 32

Duan, L.-M., Cirac, J. I., and Zoller, P. (2001). Geometric manipulation of trapped ions for quantum computation. *Science*, 292(5522):1695–1697. 65, 69

Fewell, M., Shore, B. W., and Bergmann, K. (1997). Coherent population transfer among three states: Full algebraic solutions and the relevance of

non adiabatic processes to transfer by delayed pulses. *Australian journal of physics*, 50(2):281–308. 25, 30, 32

Foot, C. J. (2004). *Atomic Physics*. Oxford University Press. 23, 93

Gaubatz, U., Rudecki, P., Schiemann, S., and Bergmann, K. (1990). Population transfer between molecular vibrational levels by stimulated raman scattering with partially overlapping laser fields. a new concept and experimental results. *The Journal of Chemical Physics*, 92:5363. 24

Gerry, C. and Knight, P. (2005). *Introductory Quantum Optics*. Cambridge University Press. 14, 17, 93

Gillespie, D. T. (1996a). Exact numerical simulation of the ornstein-uhlenbeck process and its integral. *Physical Review E*, 54:2084–2091. 71

Gillespie, D. T. (1996b). The mathematics of brownian motion and johnson noise. *American Journal of Physics*, 64(3):225–239. 71

Gulde, S. (2003). *Experimental realization of quantum gates and the Deutsch-Josza algorithm with trapped* $^{40}Ca^{+}$ *ions*. PhD thesis, University of Innsbruck, AT. 41

Häffner, H., Hänsel, W., Roos, C. F., Benhelm, J., et al. (2005). Scalable multiparticle entanglement of trapped ions. *Nature*, 438(7068):643–646. 10

He, G., Kuhn, A., Schiemann, S., and Bergmann, K. (1990). Population transfer by stimulated raman scattering with delayed pulses and by the stimulated-emission pumping method: a comparative study. *JOSA B*, 7(9):1960–1969. 24

Hensinger, W. K. (2014). *personal communication*. 90

James, D. F. and Jerke, J. (2007). Effective hamiltonian theory and its applications in quantum information. *Canadian Journal of Physics*, 85(6):625–632. 18

James, D. F. V. (1998). Quantum dynamics of cold trapped ions with application to quantum computation. *Applied Physics B: Lasers and Optics*, 66(2):181–190. 78

Jaynes, E. T. and Cummings, F. W. (1963). Comparison of quantum and semiclassical radiation theories with application to the beam maser. *Proceedings of the IEEE*, 51(1):89–109. 43, 78

Johanning, M., Braun, A., Timoney, N., Elman, V., Neuhauser, W., and Wunderlich, C. (2009a). Individual addressing of trapped ions and coupling of motional and spin states using rf radiation. *Physical Review Letters*, 102(7):73004. 9, 52

Johanning, M., Varón, A., and Wunderlich, C. (2009b). Quantum simulations with cold trapped ions. *Journal of Physics B: Atomic, Molecular and Optical Physics*, 42:154009. 45

Jonathan, D. and Plenio, M. B. (2001). Light-shift-induced quantum gates for ions in thermal motion. *Physical Review Letters*, 87(12):127901. 54

Jonathan, D., Plenio, M. B., and Knight, P. L. (2000). Fast quantum gates for cold trapped ions. *Physical Review A*, 62:042307. 54

Kayanuma, Y. (1984). Nonadiabatic Transitions in Level Crossing with Energy Fluctuation. I. Analytical Investigations. *Journal of the Physical Society of Japan*, 53:108. 33

Keaveney, J. (2014). *Collective Atom-Light Interactions in Dense Atomic Vapours*. Springer. 15

Kuklinski, J. R., Gaubatz, U., Hioe, F. T., and Bergmann, K. (1989). Adiabatic population transfer in a three-level system driven by delayed laser pulses. *Physical Review A*, 40(11):6741. 24

Landau, L. D. and Lifshitz, E. M. (1981). *Quantum Mechanics Non-Relativistic Theory: Volume 3*. Butterworth-Heinemann. 31

Leibfried, D., Knill, E., Seidelin, S., Britton, J., Blakestad, R., Chiaverini, J., Hume, D., Itano, W., Jost, J., Langer, C., et al. (2005). Creation of a six-atom schrödinger catstate. *Nature*, 438(7068):639–642. 10

Lemmer, A., Bermudez, A., and Plenio, M. B. (2013). Driven geometric phase gates with trapped ions. *New Journal of Physics*, 15(8):083001. 54

Milburn, G. J., Schneider, S., and James, D. F. V. (2000). Ion trap quantum computing with warm ions. *Scalable quantum computers*, pages 31–40. 9

Mintert, F. and Wunderlich, C. (2001). Ion-trap quantum logic using long-wavelength radiation. *Physical Review Letters*, 87(25):257904. 40, 44, 45, 80

Mintert, F. and Wunderlich, C. (2003). Erratum: Ion-trap quantum logic using long-wavelength radiation [phys. rev. lett. 87, 257904 (2001)]. *Physical Review Letters*, 91(2):29902. 40, 45

Monz, T., Schindler, P., Barreiro, J., Chwalla, M., Nigg, D., Coish, W., Harlander, M., Hänsel, W., Hennrich, M., and Blatt, R. (2011). 14-qubit entanglement: creation and coherence. *Physical Review Letters*, 106(13):130506. 10

Nielsen, M. A. and Chuang, I. L. (2010). *Quantum Computation and Quantum Information*. Cambridge University Press. 9, 58, 72

Pokrovsky, V. L. and Sinitsyn, N. A. (2003). Fast noise in the landau-zener theory. *Physical Review B*, 67:144303. 33

Rabl, P., Cappellaro, P., Dutt, M. V. G., Jiang, L., Maze, J. R., and Lukin, M. D. (2009). Strong magnetic coupling between an electronic spin qubit and a mechanical resonator. *Physical Review B*, 79:041302. 54

Retzker, A. and Plenio, M. B. (2007). Fast cooling of trapped ions using the dynamical stark shift. *New Journal of Physics*, 9(8):279. 54

Riebe, M. (2005). *Preparation of entangled states and quantum teleportation with atomic qubits*. PhD thesis, University of Innsbruck, AT. 41

Riebe, M., Häffner, H., Roos, C. F., Hänsel, W., Benhelm, J., Lancaster, G. P. T., Körber, T. W., Becher, C., Schmidt-Kaler, F., James, D. F. V., et al. (2004). Deterministic quantum teleportation with atoms. *Nature*, 429(6993):734–737. 10

Riebe, M., Kim, K., Schindler, P., Monz, T., Schmidt, P. O., Körber, T. K., Hänsel, W., Häffner, H., Roos, C. F., and Blatt, R. (2006). Process tomography of ion trap quantum gates. *Physical Review Letters*, 97(22):220407. 9

Rohde, H. (2001). *Experimente zur Quanteninformationsverarbeitung in einer linearen Ionenfalle*. PhD thesis, University of Innsbruck, AT. 41

Rohrlich, D. (2007). Berry's phase. *arXiv preprint arXiv:0708.3749*. 21

Roos, C. (2000). *Controlling the quantum state of trapped ions*. PhD thesis, University of Innsbruck, AT. 41

Roos, C. (2008). Ion trap quantum gates with amplitude-modulated laser beams. *New Journal of Physics*, 10:013002. 9

Roos, C., Riebe, M., Häffner, H., Hänsel, W., Benhelm, J., Lancaster, G., Becher, C., Schmidt-Kaler, F., and Blatt, R. (2004a). Control and measurement of three-qubit entangled states. *Science*, 304(5676):1478–1480. 10

Roos, C. F., Lancaster, G. P. T., Riebe, M., Häffner, H., Hänsel, W., Gulde, S., Becher, C., Eschner, J., Schmidt-Kaler, F., and Blatt, R. (2004b). Bell states of atoms with ultralong lifetimes and their tomographic state analysis. *Physical Review Letters*, 92(22):220402. 10

Rowe, M., Kielpinski, D., Meyer, V., Sackett, C., Itano, W., Monroe, C., and Wineland, D. (2001). Experimental violation of a bell's inequality with efficient detection. *Nature*, 409(6822):791–794. 10

Šašura, M. and Bužek, V. (2002). Cold trapped ions as quantum information processors. *journal of modern optics*, 49(10):1593–1647. 34, 42, 86

Schmidt-Kaler, F., Häffner, H., Gulde, S., Riebe, M., Lancaster, G. P. T., Deuschle, T., Becher, C., Hänsel, W., Eschner, J., Roos, C. F., et al. (2003a). How to realize a universal quantum gate with trapped ions. *Applied Physics B: Lasers and Optics*, 77(8):789–796. 9

Schmidt-Kaler, F., Häffner, H., Riebe, M., Gulde, S., Lancaster, G., Deuschle, T., Becher, C., Roos, C., Eschner, J., and Blatt, R. (2003b). Realization of the cirac–zoller controlled-not quantum gate. *Nature*, 422(6930):408–411. 9

Sørensen, A. and Mølmer, K. (1999). Quantum computation with ions in thermal motion. *Physical Review Letters*, 82(9):1971–1974. 9, 54, 91

Sørensen, A. and Mølmer, K. (2000). Entanglement and quantum computation with ions in thermal motion. *Physical Review A*, 62(2):022311. 43, 54, 72, 78, 85, 87

Terzi, N. (1998). Signatures of phonon coherent states. *Il Nuovo Cimento D*, 20(7-8):899–905. 91

Timoney, N., Baumgart, I., Johanning, M., Varón, A. F., Plenio, M. B., Retzker, A., and Wunderlich, C. (2011). Quantum gates and memory using microwave-dressed states. *Nature*, 476(7359):185–188. 11, 54, 55, 56, 61, 72, 74, 98

Timoney, N. P. (2010). *Robust rotations & coherent quantum states with a single trapped ion*. PhD thesis, Universitat Siegen, DE. 33

Vedral, V. (2003). Geometric phases and topological quantum computation. *International Journal of Quantum Information*, 1(01):1–23. 21

Viola, L. and Lloyd, S. (1998). Dynamical suppression of decoherence in two-state quantum systems. *Physical Review A*, 58(4):2733. 54

Vitanov, N., Halfmann, T., Shore, B., and Bergmann, K. (2001). Laser-induced population transfer by adiabatic passage techniques. *Annual Review of Physical Chemistry*, 52(1):763–809. 25

Wang, K., Johanning, M., Feng, M., Mintert, F., and Wunderlich, C. (2011). Quantum gates using electronic and nuclear spins of yb^+ in a magnetic field gradient. *The European Physical Journal D-Atomic, Molecular, Optical and Plasma Physics*, 63(1):157–164. 22

Webster, S., Weidt, S., Lake, K., McLoughlin, J., and Hensinger, W. (2013). Simple manipulation of a microwave dressed-state ion qubit. *Physical Review Letters*, 111(14):140501. 54, 55, 56, 57, 92, 94, 95, 98, 99

Wineland, D. J., Monroe, C., Itano, W., Leibfried, D., King, B., and Meekhof, D. (1997). Experimental issues in coherent quantum-state manipulation of trapped atomic ions. *arXiv preprint quant-ph/9710025*. 91

Wokaun, A., Bodenhausen, G., and Ernst, R. (1987). *Principles of Nuclear Magnetic Resonance in One and Two Dimensions*. Oxford: Clarendon Press. 54

Wunderlich, C. (2002). Conditional spin resonance with trapped ions. *Laser Physics at the limit*, page 261. 45

Wunderlich, C. and Balzer, C. (2003). Quantum measurements and new concepts for experiments with trapped ions. *Advances in Atomic, Molecular, and Optical Physics*, 49:293–372. 9, 15

Zener, C. (1932). Non-adiabatic crossing of energy levels. *Proceedings of the Royal Society of London. Series A, Containing Papers of a Mathematical and Physical Character*, 137(833):696–702. 31